Shale tectonic processes : Field evidence from the Parras Basin (north-eastern Mexico)

Eric Deville, Clement Dutrannoy, Julien Schmitz, Benoit Vincent, Eric Kohler, Abdeltif Lahfid

Shale tectonic processes: Field evidence from the Parras Basin (North-Eastern Mexico)

Eric Deville[1]*, Clement Dutrannoy[1-2], Julien Schmitz[1], Benoit Vincent[1-3], Eric Kohler[1], Abdeltif Lahfid[1-4]

[1] IFPEN, 1-4, av. de Bois Préau, 92 852 Rueil-Malmaison, France
[2] Present address: Veolia, 28 bd de Pesaro, 92000 Nanterre, France
[3] Present address: Cambridge Carbonate limited, 707 Warwick Rd, Solihull B91 3DA, UK
[4] Present address: BRGM, 3 av. Claude Guillemin BP 36009, 45060 Orléans Cedex, France

ABSTRACT

Major decollements located within buried overpressured shale commonly develop in thrust fronts, accretionary prisms and sedimentary deltas controlled by gravity tectonics. In seismic data, it is possible to observe only large scale deformation of what is commonly designed as mobile shale but the precise geometry and the dynamic evolution of these bodies remains poorly understood. It is often difficult to define if we are dealing with ductile or brittle deformation and to understand the role of the fluids in time and space during deformation. For this reason, large scale outcrops were studied in the Parras Basin (Mexico), which makes possible a direct observation of the shale tectonic processes. This work suggests changes in space and time of the deformation processes which occurred within the shale formation hosting the decollement. Distributed deformation was observed within the shale formation hosting the decollement compared to more localized deformation above. Also a change of the rheology of the shale over time occurred progressively toward brittle processes in the whole sedimentary pile. XRD and microscopic studies have shown that diagenetic processes are favored in the shear zones of penetrative deformation leading notably to reverse gradient of illitization. The isotopic analysis of cements in veins and the study of associated fluid inclusions have shown that fluid dynamics also evolved during time showing notably evidence for widespread fluid migration issued from rocks located below the decollement during the beginning of the deformation. Progressively, the tectonic system located above the decollement tends to be preserved from fluid migration coming from below the decollement and to be influenced only by local fluid migration (closed system).

Key words: shale tectonics, mobile shale, decollement, deformation, fluids, diagenesis
* Corresponding author E-mail address: eric.deville@ifpen.fr

Highlights:

- Outcrops were studied in NE Mexico to understand better the processes of shale tectonics
- Shale rocks deformation evolved from ductile toward brittle processes
- Fluid migrations occurred from below the decollement during early deformation
- The thrust wedge evolved progressively toward a closed hydrodynamic system

1. Introduction

In most of the tectonic fronts of convergent orogens (including accretionary prisms, fold and thrust systems in mountain belts) but also in thick deltaic systems controlled by gravity tectonics on passive margins, except when evaporates are present, decollement processes occur commonly in overpressured shale. During shale tectonics associated with this type of decollement, shale is deformed in the deepest parts close to the decollement generating poorly understood structures which are commonly named by a number of generic terms (such as mobile shale, shale diapirs, clay diapirs, mud diapirs, argillokinetic structures, etc.; Bruce, 1973; Brown, 1990; Bradshaw and Watkins, 1994; Cohen and McClay, 1996; Huh et al.,1996; Morley and Guerin, 1996; Morley, 2003; Van Rensbergen and Morley, 2000, 2003; Van Rensbergen et al., 2000, 2003a and b; Corredor et al., 2005; Briggs et al., 2006; Deville et al., 2006, 2010; Wiener et al., 2010; Elsley and Tieman, 2010). These terms are currently used to describe geometric features on the seismic data but with only geophysical data and without direct constraints provided by wells or field observations, it is difficult to define exactly what are the prevailing deformations processes which occur within these shale-rich bodies (see an example in. 1). These volumes of sediments poorly imaged in seismic data are commonly considered as mobile shale bodies but generally, authors do not prejudge about the nature, the structure and the genetic processes at the origin of the deformation of these shale-rich bodies. Present-day understanding of subsurface clay-rich sediment deformation remains relatively low and commonly made by comparison with the larger literature on salt tectonics (Morley and Guerin, 1996). However, these processes clearly differ from salt mobilization, notably by the crucial role taken by the fluid dynamics that is able to induce sediment liquefaction and controls overpressured shale deformation. In most cases, on seismic lines, it is difficult to define if sediment deformation occurred as a brittle or a ductile process, even though this implies drastic differences in the rheology of the material involved and the modes of deformation (see discussion in Wood, 2010, 2012). When interpreting seismic data, what is usually designated as mobile shale corresponds to volumes of rocks whose global geometry suggests a ductile deformation (pillow shapes, deformed cores of large anticlines suggesting diapiric shapes). It is generally difficult to define if this deformation occurred as liquefaction of sediments, or as flow of ductile but still stratified material or else as deformation of intensively fractured rocks at depth (Deville et al., 2003; 2006; 2010). With the improvement of seismic data, it progressively appeared that what was considered as shale diapir is much more restricted than previously thought (Van Rensbergen et al., 2003).

The widespread occurrence of shale tectonic processes, their common association with hydrocarbon producing areas and their influence on the development of a wide range of sedimentary basins require new studies of these phenomena. For a better understanding of the deformation processes of what is commonly named mobile shale, we made field studies on an outcropping case. The objective of this work was to study outcrops associated with a major decollement zone in shale located at the base of a thick tectonic wedge. In active or recent thrust systems developed on top of a decollement in shale or on top of intensively deformed shale, because of the burial, it is usually impossible to study the shale deformation directly on wide surface outcrops. For this reason, we choose a case study in the Parras Basin in northern Mexico (Fig. 2), which corresponds to an area where exposures of a large decollement system can be studied thanks to a late uplift and erosion (Figs. 3, 4). The objective of this study was to better understand the deformation mechanisms of the so-called mobile shale notably close to the decollement level and in the cores of clay-rich anticlines, as well as the scale factors (microstructures *vs.* macrostructures). We also wanted to use this outcropping analog to better understand the interactions between deformation - migration of fluids - diagenesis in tectonic fronts characterized by decollement in shale.

2. Geological framework

2.1. Depositional setting

What is commonly named the ‘Parras Basin’ is a part of the Mexican Laramide tectonic front which includes the deltaic uppermost Cretaceous and Early Tertiary terms forming the detrital stratigraphic series of the Jurassic-Cretaceous of the Sierra Madre Oriental in the area of Parras and Saltillo (Figs. 2, 3). The Parras Basin develops south of the Popa and Sabinas basins and it is limited to the northwest by the Coahuila platform and to the south by the front of the Sierra Madre Oriental (Weidie et al., 1966, 1978; Weidie and Murray, 1967; McBride et al., 1971, 1973, 1974, 1975; Tardy et al., 1975; Tardy, 1980; Soegaard et al., 2003) (Fig. 2, 3). The area studied in the Parras basin shows wide outcrops partly hampered by the development of recent alluvial systems. The cores of the anticlines and the lower part of the series, which includes highly deformed shale, outcrop in good conditions on several hundred of km^2 (Fig. 4). The oldest rocks present in the study area which form the stratigraphic base of the Parras basin correspond to the Cretaceous carbonate of the Coahuila group (Lehmann et al., 1999; Lawton et al., 2001). The sedimentary base of the Parras basin consists of Campanian marine shale (Parras shale formation; McBride et al., 1974; Bartolini et al., 1995, 2001; Ifrim et al., 2015). Above, the sediments of the Parras Basin correspond to a deltaic system (Difunta group; Murray et al., 1959; 1960; 1962) essentially of Maastrichtian age and for a minor part of Paleocene age (Fig. 5). The Difunta Group corresponds to a succession of stratigraphic cycles (Warning and McBride, 1976; Wollenben, 1977; Soegaard et al., 2003; Fig. 5). The various formations correspond to different sedimentation areas sourced by clastic inputs, from the upstream deposits of a flood plain to a downstream turbidite system. This paleo-delta was sourced by the erosional products of the Sierra Madre structured during the Laramide period. During Campanian-Maastrichtian times, the Parras Basin was located at the connection between the Western Interior Seaway of the North American continent and the Gulf of Mexico (Robinson-Roberts and Kirschbaum, 1995). At that time, this area was part of a large continental shelf open towards the Gulf of Mexico to the east and bordered to the west by the arc of the Sierra Madre. The thick accumulation of the sediments of the Difunta Group, up to 6000 m (McBride et al., 1975), was probably related to a flexural basin installed on a thinned continental crust which corresponded to the western margin of the Gulf of Mexico. The common absence of fragments of carbonates in the sandstone Difunta Group shows that the carbonated reliefs of the Sierra Madre Oriental were not the source of the clastic input in the Parras Basin. The delta was most probably fed by a fluvial system which brought the material from the magmatic rocks of the Sierra Madre Occidental (Guerrero arch) to the west. Deltaic series are composed of fine to very-fine-grained sandstone with some exceptional layers of medium-grained sandstone. Periods of eustatic drop result in forced regressions whose deposits (shoreface and fluvial deposits of the Las Imagenes and Las Encinas formations) correlate across the basin for tens of kilometers (Soegaard et al., 2003). On top of the Parras shale, a first progradation of the delta shows that the Upper Campanian clastic input issued from the erosion of the reliefs of the Sierra Madre were initially too high in volume compared to the available space. This prograding series is designated as the Cerro del Pueblo formation in the literature and it is late Campanian in age (McBride, 1974; Eberth et al., 2004; Vega et al., 2018). The transition Campanian-Maastrichtian is located at the top of the Cerro del Pueblo which is consistent with the data published by McBride et al. (1974) and Vega et al. (2018). Above the shoreface of the top of the Cerro del Pueblo formation, beach deposits are capped with red fluviolacustrine continental series deposited in a delta plain (up to almost 1000 m thick). This unit is mentioned as the Cerro Huerta formation in McBride et al. (1974; 1975). On top of the Cerro Huerta formation, a gradual transgression led to the deposition of marine shoreface series. This frankly marine episode is designated as the Cañon del Tulle formation (McBride, 1974). The maximum flooding surface of this transgression is situated in deep marine clays-rich layers. Thin turbidite systems developed during the following period of high sea level, probably sourced by hyperpycnal flows generated by seasonal flooding of rivers upstream. On top of these turbidite systems, a new regression is correlated with an important eustatic fall (about 50 m) during Upper Cretaceous. This forced regression caused the deposit of sandy shoreface systems directly on top of deeper marine deposits. This corresponds to the Las Imagenes formation, which includes sandbars tens of kilometers long.

Then, a new transgression (Cerro Grande formation) was associated with more marine deposits (shallow marine clays) punctuated by several minor episodes of regression (prograding shoreface). On top of these marine deposits, a new forced regression (Las Encinas formation) induced shoreface and then red fluvial sandstones deposition which form a strong and distinctive bar. It marks the transition to the Paleocene (McBride et al., 1974; Diaz et al., 2017; Vogt et al., 2016; Martinez-Diaz et al., 2017; Vega et al., 2018). Higher up in the series, a last transgression was responsible for the deposition of deep marine deposits (Rancho Nuevo/ Potrerillos formation) which consist of marine shale punctuated by gravity flow deposits that form tabular zones at the top of the series of the Parras basin.

2.2. Tectonic framework

The study area corresponds to the Laramide front that was mostly active during Early Tertiary times (McBride et al., 1974). At that time, the compressive front of the Sierra Madre Oriental extended on the western margin of the Gulf of Mexico. During the Neogene, the entire western edge of the Gulf was uplifted (especially along the arch of Tamaulipas), which led to erosion responsible for the outcrop of the former compressive structures (McBride et al., 1974; Gray et al., 2001). The Eastern Parras Basin is preserved in a large syncline trough showing a north-south axis (Fig. 3), the edges of this trough being largely eroded (especially the western edge situated beside the Coahuila arch; Fig. 3, 4). Therefore, it is possible to study directly wide outcrops corresponding to a complete geological section of the Parras basin resulting of the Laramide compression (Fig. 4). As it has been originally proposed by Tardy et al. (1975), a generalized decollement occurred within the Parras marine shale. Indeed, the deltaic system of the Parras Basin was affected by intense deformation including decollement tectonics in Campanian marine shale (Parras shale formation). In the area, the Early Cretaceous sediments are only involved in long wave-length folding (Coahuila block), whereas the Upper Cretaceous-Paleocene is deformed in a system of folds and thrusts (see especially the mapping made by McBride et al., 1974, 1975, Tardy et al., 1975 and Tardy, 1980). Along section of Fig. 3B, the shortening is estimated to be higher than 10 km. The deformation related to decollement tectonics occurred in marine open environment and the related structures were progressively covered by marine sediments towards the tectonic front (marine clays and turbidite deposits gravity and mass flows, *e.g.* Paleogene Rancho Nuevo or Potrerillos formation; Fig. 4). The age of the decollement is then known thanks to the presence of these growth layers of Paleocene age covering the tectonic front (Lawton et al., 2001). Indeed, the latest layers preserved in the Parras Basin correspond to siliciclastic deposits dated of Paleocene age, *e.g.* Potrerillos formation of the Mac Bride et al. (1974) or Rancho Nuevo of Soegaard et al. (2003). This formation shows fan geometries which are compatible with syntectonic sedimentation. As a consequence, the deposition of this formation can be considered as coeval to the observed deformation in the Parras Basin (Late Maastrichtian-Paleocene deformation).

3. Material and methods

A sequence of different approaches has been used to characterize deformation, fluid migration and diagenesis: field structural geology, optical microscopy of veins, XRD of clays, study fluid of inclusions in calcite and quartz, stable isotope composition of carbonate cements, study of organic matter maturity (using Rock-Eval and Raman techniques) and thermal modeling. The objective of this work was to better understand the evolution of the deformation processes, their physical conditions, and to identify the nature and origin of the fluids associated with this deformation. Large scale field mapping supported with Landsat and Spot satellite imagery was made NW of Saltillo (Figs. 6, 7). This field study included also microstructural observations and measurements.

Veins have been studied by optical microscopy including catholuminescence. Petrographic investigation includes optical microscopy performed on half-stained thin sections (Alizarin red S + potassium ferricyanide; Lindholm and Finkelman, 1972), and cathodoluminescence (CL; Machel, 2000).

After extraction of the fine fraction, with a particle size of less than 2 µm, the X-ray measurements were carried out on oriented preparations which are air dried or saturated with ethylene glycol. Saturation with K or Mg followed by ethylene glycol (EG) solvation is a classical method used to identify high-charge smectite. XRD patterns were acquired using Cu radiation with 0.017°2θ step size and $91s.2\theta^{-1}$ counting time with a position-sensitive detector on an X'pertPro Panalytical diffractometer. For the identification of minerals in a rock and clays characterization, X-ray profiles are acquired in Bragg-Brentano geometry. The identification of minerals is achieved using the crystal-chemical database from the Mineralogical Society of America and the Crystallography Open Database (COD).

A thermobarometric reconstruction of the diagenetic history was carried out by the study of fluid inclusions in the different generations of cements filling veins (including calcite and quartz) to define the composition and temperature-pressure conditions of the fluid having circulated in the Parras Basin since the end of the Cretaceous. This study attended to characterize the physical conditions of the different fluids that participated in the mineralization of diagenetic phases and to better understand the interactions between deformation processes, fluid migration and diagenesis (Roedder, 1984; Shepherd et al., 1985; Goldstein, 2001). Microthermometry measurements were made with a Nikon eclipse LV100 optical microscope using a video system connected to a computer coupled to a Linkam turntable THMSG 60. Cooling was ensured by a circulation of liquid nitrogen. Calibration was made at -56.6°C with a quartz sample of Calanda containing inclusions of pure CO_2.

Isotopic analyses of carbonate cements in mineralized veins were performed on cements from fractures localized in the carbonates of the Coahuila Group and above these carbonates, in the Parras shale formation, below, within, and above the decollement zone. Carbonate powders were sampled with a microdrill under a binocular from the calcite spars and the cataclasites. They were reacted with 100% phosphoric acid (density >1.9, Wachter and Hayes, 1985) at 75°C using a Kiel III online carbonate preparation line connected to a ThermoFinnigan 252 masspectrometer. All values are reported in per mil relative to V-PDB by assigning a $\delta^{13}C$ value of +1.95‰ and a $\delta^{18}O$ value of -2.20‰ to NBS19. Reproducibility was checked by replicate analysis of laboratory standards and is better than ± 0.02 (1σ).

73 Rock-$Eval_6$ analyses (Lafargue et al., 1998) were made in the study area and among them 58 were made on samples from the Parras shale formation (where the decollement is located) and the others on samples from the formations which are stratigraphically located above the Parras shale formation (see supplementary material; table SII).

Paleothermometry by Raman Spectroscopy of Carbonaceous Material (RSCM) was applied on four selected samples located in the decollement zone and just above (samples 8B, 11, 120C, 113C; Fig. 6A). RSCM is a method based on the structuration degree of the residual

organic matter to estimate the thermal peak undergone by rock samples. This method was initially developed in the range 300-700°C by Beyssac et al. (2002). The method has been then expanded to be used for lower thermal conditions in the range 150-300°C (Lahfid et al., 2010). RSCM method allowed completing Rock-Eval results for high maturity values.
Temperatures defined by microthermometry and Raman spectroscopy were finally used to reconstruct the burial history of the Parras Basin by 1D modeling performed with the GENEX-GENTECT software®. The location of the 1D model has been chosen at the place where samples 64A and 68A were collected (Fig. 6B). The data used for the modeling include lithostratigraphic descriptions of each formation, their thickness and the estimated erosion as summarized in Fig. 6B. Thermal parameters of these formations were chosen taking into account their lithology from the default data base of the GENEX software.

4. Results

4.1. Deformation processes in and around the decollement zone

The Cretaceous carbonate formations of the Coahuila arch which are located below the decollement zone are affected by long wave-length folding processes contrary to the formations located above the decollement (Figs. 3, 4, 6, 7). In the area studied, they are simply tilted towards the east or south-east (Figs. 3, 4, 6, 7). They are simply tilted towards the east or south-east. They show evidence of intense fracturing associated with well-developed calcite cements (Fig. 8). Outcrops of Cretaceous Parras shale located below the basal decollement show a well-preserved continuous stratification and abundant fractures perpendicular to the stratification and dispersed in direction (Fig. 8). Dips of the beds of the lower Parras shale show a conform bedding to those of the carbonates of the Coahuila arch (tabular levels tilted towards the east and south-east due to the Coahuila arch doming). The decollement level is located at the base of the Parras formation in the southern part (inner zone), while it is located higher in the stratigraphic series close (less than a hundred meters) to the lower sandstone formation (C. del Pueblo) north of the study area (outer zone toward the tectonic front). The outcrops observed in the basal decollement zone are characterized by several meters of intensely sheared rocks, cataclastic carbonate rocks and tectonic breccias (Fig. 9). In many places, diagenetic concretions are observed in the form of centimetric to decimetric rounded calcium carbonate concretions and tubes corresponding probably to former fluid circulation conduits in the fracture system (Fig. 9). Rocks located above the decollement show evidence for former percolation of fluids, which are characterized either in a very diffuse way in the argillaceous rocks, or more focused in shear planes or in the form of fluid chimneys (Fig. 10). Gradually, above the basal decollement, intensely deformed clay-rich areas are encountered showing a scaly fabric where the initial stratification is no longer visible. The initial stratification can only be recognized from the alignment of boudinated layers of sandstones preserved in clay-rich masses (Figs. 10, 11; Figs. S2). Obviously, the clay-rich levels were affected by strong creeping, while the sandstone beds ruptured in different strands. These structures are clear evidence of a period of ductile deformation of shale rocks. Subsequently to the ductile deformation, shale rocks were intersected by fault planes associated with calcite cements (Fig 12).

The shale-rich core of the main folds. In the study area, several structural zones can be distinguished (Fig. 3, 4): (1) an outer area of relatively tight frontal folds related to an imbricated stack of thrust sheets, (2) an area transported with relatively little deformation only marked by reverse faults with moderate throws, and (3) an inner large wavelength folds area. As mentioned above, the main basal decollement level located in the Parras shale propagated up in the stratigraphic series toward the north. Consequently, there are large volumes of Parras shale which are deformed in the core of the folds the southern part of the study area (more than five hundred meters thick). The cores of the main folds do not show thick continuous sandstone beds. The center of the main folds of the studied area consists mainly of scaly-fabric shale where the initial stratification can only be recognized very punctually from the boudinage of few recognizable sandstone beds (Figs. 10, 11; Figs. S2, S3 in supplementary material). In most cases, even sandstones failed to inform us directly about the initial stratification as they correspond to isolated boudinated elements in shale-rich masses (Figs. 10, 11; Fig. S3). Only traces corresponding to shale welds between the boudins are visible within the shale rocks (Fig. 10; Fig. S3). Also, in many places, we observed probable former conduits of fluid flows in the form of concretion tubes of several of centimeter of diameter with a complex geometry, generally made of sandy-argillaceous rocks cemented by carbonates (Figs. 10, 11). Very characteristically, the core of the main folds of the study area was the place of an intense penetrative deformation in the early stages of folding. In contrast, during the progressive evolution of the deformation, the cores of the folds were affected by brittle processes associated with striated calcite precipitation in the fault planes (Fig. 12). Therefore, the cores of these main folds were the place of a rheological change characterized by an evolution from intensively penetrative deformation to localized brittle deformation.

Contrary to the core of the folds, stratifications are well-preserved In the post-Parras shale formations where thick sandstone beds are continuous and only little deformed (Figs. 13, 14). The transition between the scaly shale and the continuous sandstone beds is sharp (few meters) and it is probably mainly controlled by the initial lithology before deformation, the penetrative deformation being principally localized in areas with little sandstone levels. In the upper part of the marine Parras shale formation stratifications are perfectly preserved and the dips are consistent with those of the overlying formations (especially with the formation Cerro del Pueblo).

Fracture systems. Above the basal decollement, numerous low dipping faults corresponding to localized mineralized shear bands (several centimeters to several tens of centimeters thick) developed in the lower part of the thrust wedge (Fig. 15). These planes show slickensides made of calcite (Fig. 16). These faults are either parallel to the bedding (flat areas), or slightly oblique to the stratification (ramp areas). In some places, transitions from flat to ramp can be observed (Fig. 15). The slickenlines have a well-regulated average strike of N15° (Fig. 16). This direction is interpreted as the main transport direction during the main deformation phase (north verging). Frequently, the striated calcite planes are affected by open subvertical fractures, roughly perpendicular to the direction of displacement (Fig. 16). In many cases, we observe recurring figures showing that flat shears with calcite crystallization are located a few centimeters just above sandstone beds (Fig. 15).

Many cataclasites layers are connected with the low angle fault planes. Either they occupy part of the fault plane (in this case the fault zone includes a well-preserved crystalline calcite part and a cataclasite part) or they appear in the fault planes as pillows that can form locally several meters thick lenses (Fig. 17). These pillows are interpreted as mobilization of the cataclastic material as injectites which has been displaced in the fault plane and locally accumulated in lenses. The cataclastic material is made of mechanically crushed calcite partly re-cemented by calcium carbonate cements. These lenses of cataclasites contain frequently polygenic breccia elements issued from the surrounding rocks forming real tectonic breccias (Fig. 17). In different places, we observed sedimentary sandstone dikes. Some of them are tightly folded in a way that reflects a flattening perpendicular to the horizontal plane. We interpret the setting of these dikes as occurring in an early stage, at least prior to the main compaction of the surrounding clays-rich sediments (Fig. S1 in supplementary material). The study of fractures which are related to the main tectonic event has shown that the calcite-cemented fractures have clear orientation changes between areas in the decollement zone and the fracture system observed above the decollement zone. In the lower part of the thrust wedge which is essentially made of shale-rich sediments associated with small sandstone beds, the subvertical fracture have an average orientation perpendicular to the direction of transport observed on the low angle fault planes (Fig. 14). In the few thin sandstone beds (< 10 cm thick), however, fracture networks are generally conjugated with an angle of about 40° with respect to the direction N15°. Fractures located in the upper part of the thrust wedge are dominantly subvertical with the same direction as the slickenlines along the fault planes (roughly N15°) which is interpreted as the direction of shortening (Fig 14). These subvertical fractures are filled with calcite on top of the Parras shale formation and the Cerro del Pueblo formation. However, above the clay-rich layers of the Cerro Huertas formation, these fractures are still well-expressed with the same dominant orientation N15° but they are no longer filled with thick calcite cements.

4.2. Syn-kinematic diagenesis

Veins. The study by optical microscopy and CL has shown several generations of syn-kinematic diagenetic veins. The following sequence of mineral precipitation was distinguished (Fig. 18): *1) Calcite.* Large early veins filled with calcite cements have been observed in the Cretaceous carbonates of the Coahuila group, as well as in the different structural levels distinguished in the Parras shale formation (Fig. 19). In the Coahuila group, these veins correspond to an early generation of large calcite crystals very commonly twinned and often distorted and showing a faint sector zoning under CL, despite an overall dull brown homogeneous luminescence. The host rock appears intensively affected by open fractures, with a rather isotropic distribution. These large calcite veins are also present in the decollement zone and above. Some calcite bands locally exceed 50 cm of thickness. These veins are also well-developed at the top of the Parras shale formation and the Cerro del Pueblo formation where they are made up mainly of large subvertical open fractures oriented mainly N15° (see above). We did not observe such massive veins above the Cerro Huertas formation. *2) Cataclasites.* The calcite veins have been deformed (minerals are often folded), sheared (shear bands within calcite cements) and, in many cases, the calcite cements have been crushed generating cataclasites (Fig. 20). These cataclasites bodies locally include brecciated polygenic elements from the surrounding rocks from macrocrospic to microscopic scale. *3) Quartz.* Subsequent to the development of cataclasites, mostly quartz precipitation occurred. Quartz is expressed either by large euhedral crystals, or as microcrystalline veins.

Quartz veins were either newly formed or they re-used the former calcite veins (Fig. 21). In the latter case, the quartz veins are located either at the walls of the early calcite veins that are re-opened, or in the core of the calcite veins propagating at the calcite crystal boundaries. Some quarz crystals are sheared which shows also the syn-kinematic character of these late silica precipitations. The study of the calcite cements present in the faults and open fractures of the Parras Basin reveals a homogeneously dull brown luminescence, and faint sector zoning under CL, only visible within some of the least deformed/sheared/crushed crystals.

Clays. XRD study has shown that a general process of clay transformation follows, from the top to the bottom of the Parras Basin, a general trend to illitization and chloritization of smectites, which is a very classic pattern of diagenetic transformation. Illite and chlorite are widespread in the Parras formation inside the study area. More specifically, it has been possible to demonstrate that diagenesis is not only influenced by the general conditions of temperature and pressure in relation to the sedimentary burial, but strain also plays a role on clay diagenesis. We observed that penetrative deformation process has the effect of accelerating the process of illitization and chloritization. Indeed, in the decollement zone, deformation was focused on surfaces of discontinuity corresponding to shear planes currently mineralized by calcite precipitation. Clay-rich portions between these shear planes are little deformed and mineralogical transformations are moderate. However, in the corridors of penetrative deformation (well-developed cleavage), mineralogical changes are intense and the vertical gradient of illitization is not respected anymore. In these areas, electronic microprobe mapping has shown that diagenesis is characterized by a strong illitization and chloritization of smectite, and jointly with an increase in the quartz content, and less calcite content compared to the clays-rich layers in the decollement zone (Fig. 22). This increase of diagenetic transformations in areas of penetrative deformation generates locally inverse gradients of illitization and chloritization. Such a feature is notably observed between the decollement zone and the cleavage corridors located above the decollement zone where deformation controls partly diagenesis (Fig. 22). Sample 65 in the lower zone is characterized by the presence of a large quantity of smectite and well-ordered illite-smectite interlayer visible with the presence of broad lines around 15 and 18 Å and the importance of the variations in line positions of the air dried (AD) and ethylen glycol (EG) profiles (blue and purple lines respectively and blue arrows to illustrate diffraction line displacements).. Sample 63 in the intermediate zone is characterized by the presence of chlorite and illite and a small amount of illite-smectite interlayer visible with the presence of fine lines around 14, 10 and 7

Å and the small variation of positions of the lines of the AD and EG profiles (brown and red lines respectively). Sample 60 in the upper zone is characterized by the presence of chlorite and illite and a small amount of illite-smectite interlayer. The variation of the positions of the lines of the profiles AD and EG (green and orange lines respectively) is very small.

More generally, Scanning Electronic Microprobe study of scaly shale has shown that the initial fabric of their protolitic matrix does not show preserved stratigraphic layering. The only oriented fabric which is visible in the scaly shale corresponds to late microfractures in which calcite has precipitated. Clay minerals have recrystallized mainly to illite. Scattered patches of quartz and albite have also developed in the scaly shale (Fig. 23).

4.3. Fluid inclusion microthermometry and barometry

The petrographic study of selected samples revealed that inclusions are present in calcite cements and in some cases in quartz cements (Fig. 24). Microthermometry measurements were performed on fluid inclusions trapped in these two types of minerals. It was possible to distinguish four types of fluid inclusions trapped in calcite or quartz minerals (Fig. S5, S6; in supplementary material): *Type 1* corresponds to isolated primary fluid inclusions dispersed in quartz and calcite minerals. They are sub-rectangular with dimensions ranging from 3 to 8 µm and they are all two-phase (liquid and vapor phases; Fig. 24). *Type 2* corresponds to primary fluid inclusions ranging from 3 to 8 µm in size with various shapes. These inclusions are single-phase gaseous inclusions and they look darker than the aqueous inclusions. These inclusions are present in calcite and quartz. *Type 3* corresponds to rectangular aqueous fluid inclusions aligned along calcite twins. These inclusions are late primary to secondary inclusions with dimensions between 2 and 5 µm. *Type 4* correspond to generally aligned secondary fluid inclusions (in fracture scar) of rectangular shape for the biggest and round for smaller. The rectangular inclusions have a size of about 2 to 3 µm and are most abundant. They are two-phase (liquid and vapor phase). Only primary inclusions of types 1 and 2 having a size greater than 3 µm were used for the microthermometry study presenter here.

Determining the first melting temperature (T_{fm}) and the final melting temperature (T_{mi}) of ice (low-temperature microthermometry) in the aqueous inclusions gives information on the composition of the fluid trapped in the inclusions and thus, for aqueous inclusions, the presence and the content of dissolved species. For all samples, first melting temperature (T_{fm}) values were obtained between -53° and -49°C (Table 1; Fig. S7 in supplementary material). These temperatures correspond to the eutectic temperature of a H_2O-$CaCl_2$ system which is consistent with the fact that the inclusions are present in carbonates (Bowers et., 1983). Temperatures of final melting (T_{mi}) gave an estimate of the salinity of the fluid. In calcite, T_{mi} display a wide range with statiscal tendency towards a dominant window between -2°C and 0°C (Table 1; Fig. S8 in supplementary material). This suggests the presence of slightly saline water (Fisher, 1976). Eventually, this could be related to the presence dissolved CO_2 in the inclusions which lower the melting point of water, but it was not possible to characterize the presence of clathrate in the inclusions. However, the small size of the inclusions is not favorable to identify the presence of CO_2 clathrate. Values of T_{mi} slightly greater than 0°C correspond probably to a metastable state of the fluid inclusions. Fluid inclusions in quartz have T_{mi} close to 0°C which is compatible with almost fresh water compositions. The homogenization temperatures (T_h) observed in the liquid phase have been measured with an uncertainty of +/- 2°C (Table 1; Fig. 24). T_h corresponds to the liquid-vapor transition.

Considering the quite wide range of homogenization temperatures of the acquired distribution per samples, modal temperatures were chosen as references in the following discussion (Table 1; Fig. S9 in supplementary material). T_h of primary fluid inclusions measured in the different samples range from 125 to 185°C in the calcite cements and reach maximum values of 230°C in quartz cements. T_h evolves with the temperature of trapping. However, T_h are not necessary equal to trapping temperatures depending on the confining pressure. In samples 64A and 68A samples, trapping temperature was evaluated from cogenetic inclusions. Methane-rich inclusions were observed in samples collected in the decollement zone (samples 64A and 68A). They have been observed in calcite and in quartz minerals. Methane can be identified by phase transition close and below critical temperature of -82°C. For methane-rich inclusions, the T_h is between -92°C and -94°C (Fig. S10; in supplementary material). These inclusions were used to determine the temperature and pressure of trapping of the fluid in these samples (Mullis, 1979). The density has been determined from the saturation curve of methane (Hanor, 1980) and state equations MRK (Angus et al., 1978). The density values obtained from Angus' et al. (1978) model are 0.292 g/cm^3 at -92°C and 0.301g/cm^3 at -94°C. This allowed us to draw methane isochores between 50 and 300°C (Setzmann and Wagner, 1991) to determine the pressure within these inclusions for the T_h of the aqueous inclusions.

The P-T conditions of the studied samples correspond to relatively high pressure and high temperature. In sample 68A, aqueous inclusions containing dissolved methane in HP-HT conditions, it can be considered that they are saturated with dissolved methane. Thus, in this case, T_h can be considered as equivalent to the temperatures of fluid trapping (Roedder and Bodnar, 1980; Roedder, 1984). The temperature and pressure conditions identified in the sample 68A (Fig. 25) indicate that the fluids were trapped in the quartz crystal at a temperature of 220+/-10°C and pressure between 1380 and 1480 bars. In calcite, the trapping temperature is 170+/-10°C and pressure between 1200 and 1280 bars. Quartz forming later than calcite, it recorded higher temperatures due to a higher burial. These values show that calcite and quartz precipitated both in overpressure condition with a resulting increase of about 26°C per 100 bar between calcite and quartz precipitations following the isochores published by Setzmann and Wagner (1991; Fig. 25). In the other samples analyzed (107B, 132, 83), in order to propose an approximation of the trapping temperatures as a function of T_h, a correction was performed (Table 1) based on an estimate of the confining pressure of each sample deduced from an estimate of the erosion amount as summarized on the structural section of Fig. 6B and from the isochore curves of the H_2O-CO_2 system (Fig. 25).

4.4. Isotopic analyses of carbonate cements

Carbonate micrite matrix of samples of the group of Coahuila shown $\delta^{18}O$ of about -10‰ vPDB and slightly positive values for $\delta^{13}C$ vPDB (Table S_{II}, in supplementary material). These measured values very probably reflect a thermal re-equilibration during burial of initially marine carbonates, which is consistent with the deep structural position of these carbonates (Fig. 65, 27). The analyzes of carbonate cements in the carbonate of the Coahuila group, in the decollement zone, in the carbonate pipes and in the veins of fractures within the sediments located above the decollement show very constant $\delta^{18}O$ values and decreasing $\delta^{13}C$ values from the Coahuila carbonate rocks to rocks located above the decollement (Fig. 26). $\delta^{18}O$ and $\delta^{13}C$ values of veins located above the decollement show a remarkable clustering, this regardless of the structural position and orientation of the fractures. $\delta^{18}O$ values are ranging between -9 and -11‰ vPDB and $\delta^{13}C$ values are ranging between -2 and -6‰ vPDB. In these veins, the values of $\delta^{18}O$ are fully comparable with those measured in the Coahuila carbonates. In contrast, values of $\delta^{13}C$ are much lower in the calcite cements than in the carbonates of the Coahuila group, indicating enrichment in light carbon likely related to the influence of hydrocarbon-derived ^{12}C. In addition, the isotopic values measured in cataclasites show significantly higher $\delta^{18}O$ values than those measured in crystalline calcites. The few samples showing very low values in $\delta^{13}C$ (-10 to -11‰ vPDB) correspond to cements that delivered hydrocarbon inclusions.

4.5. Rock-Eval 6 analyses

In rock Eval 6 pyrolysis technique, the hydrocarbons liberated during the progressive heating are measured with a FID detector (Flame Ionization Detector) and form the peak S1 (representing the free thermo-vaporized hydrocarbons) and the peak S2 (products of pyrolysis during cracking of organic matter). In the studied samples, the peaks S1 are either nil or very low (probably remaining traces of hydrocarbon gas). S2 peaks are also very low, hardly measurable in the Cerro Grande formation and in the Canon del Tulle formation (Table S_{II}, in supplementary material). T_{max} is a function of the maximum temperature of the S2 peak and it corresponds to a maturity index of organic matter. We obtained T_{max} values of 460°C in the Cerro Grande formation and between 483 and 495°C in in the Canon del Tulle formation, which correspond to high maturities of organic matter (gas window). In the Parras Shale formation, S2 and so T_{max} are not measurable (T_{max} > 500°C; equivalent to VRo > 1.7%) instead of the presence of residual carbon (Table S_{II}, in supplementary material), which is characteristic of very high maturities (overmature organic matter). The residual carbon constitutes most of the total organic content in all the studied samples. Therefore, these data have shown that the organic matter which is in the Parras shale is the gas window or overmature in the whole study area. This demonstrates that gas has been generated in the Parras shale of the studied area.

4.6. Raman spectroscopy (RSCM geothermometer)

The temperatures obtained by the RSCM method in scaly 'mobile' shale rocks just above the decollement zone and in the core of the main folds (samples 8B, 11, 120C, 113; location in Fig. 6A) gave values in the range 180-220±10°C (Fig. S11 in supplementary material). These results are consistent with those obtained using Rock-Eval techniques and from the study of fluid inclusions in quartz which very probably crystalized during the thermal peak. Notably, sample 120C (north of sample 68A; Fig. 6A) gave RSCM temperature of 220± 10°C and similar temperature deduced from fluid inclusions in quartz in sample 68A. The thermal peak measured within the 'mobile' shale inside the core of the large folds gave RSCM temperatures between 180 and 190± 10°C (samples 8A, 11 and 113; Fig. 6).

4.7. Thermal modeling

Temperature is a parameter which evolves directly with burial and uplift during tectonic events. The thermal model used in this study simulates the stratigraphic back-stripping and the tectonic thickening and subsequent uplift history (Fig. 28). To fit the model with the paleothermometric results, notably the peak temperatures in specific formations which were estimated by fluid inclusions in quartz crystals and RSCM method in shale in the decollement zone, we had to choose a heat flow 50 mW/m^2 at the base of the section taking an average constant surface temperature of 20°C. Modeling results suggest a significant temperature increase in the Coahuila and Parras formations during the compressive tectonic phase which is responsible for the decollement within the Parras shale. The model shows that the thermal peak occurred just after fault activity (during late Paleocene times) and reaches about 180°C at the top of the of Parras formation and 240 to 250°C at the top of the Coahuila carbonates (Fig. 28). These results concerning the timing of the temperature peak are in good agreement with those of the study of Gray et al. (2001) from apatite fission track and apatite helium dating made at a regional scale.

5. Interpretation

This study of a wide scale tectonic wedge affected by a major decollement located in a shale-rich formation has shown that this system evolved through different steps as summarized in Figs. 29 and 30. Combined studies including field geology, XRD, SEM, microthermometry and barometry on fluid inclusions, isotopic study of carbonates, Rock-Eval and RSCM measurements and thermal modeling made possible to identify the following major stages concerning the history of deformation - fluid migration - diagenesis relationships of the site studied which probably occurred during a progressive continuum of deformation.

Stage A: Early diagenesis related to sedimentation. During the deposition of the deltaic system, the early stages of diagenesis were characterized by a transitional transformation of clays, from the top to the base of the delta system, with illitization and chloritization of smectite (mainly genesis of interlayered illite-smectite). Such trend was observed all over the study area (Fig. 6). The development of syn-compaction sedimentary dikes probably occurred during this initial stage of diagenesis.

Stage B: Scaly shale and early folds. The older compressive deformations affecting shale rocks have generated a penetrative scaly fabric within parts of the Parras shale formation. We consider these layers as comparable to what is commonly considered as mobile shale. Most of the penetrative deformation was observed in areas which are very poor in sandstone layers. In areas containing numerous sandstone horizons (even thin), folds and fractures were observed but no evidence for penetrative deformation. Penetrative deformation developed essentially in the inner part of the study area (southern part), in the shale located today immediately above the basal decollement or in the core of the large folds. The penetrative deformation of shale occurred in the domain of transformation of smectite to illite and hydrocarbon gas generation (Fig. 29, 30). This penetrative deformation is not always located in the same stratigraphic horizon (Fig. 6B, 7). This process initiated the structure of the core of the major folds made of deformed shale with stretched and discontinuous sandstone beds inside. In the inner part of the study area (the deepest part during deformation), large tectonic accumulations of deformed clay-rich material can be regarded as detachment folds. It was found that there were both, spatial and temporal evolutions of the rheology of the shale-rich layers; the rheological behavior of shale varied over time (unlike decollement in evaporites for example) and penetrative deformation was localized in certain preferred areas (as opposed also to evaporite levels in which the deformation is much more distributed).

Stage C: Decollement propagation and deep fluid flow. Within the clay-rich formation that hosts the decollement, the deformed shale observed above the decollement zone and in the core of the folds did not act, neither in time nor in space, with a uniform constant rheology. Indeed, deformation mechanisms in shale evolved over time. Clearly an evolution of the deformation mechanisms occurred from a penetrative ductile process to a brittle behavior (faulting overimposed on early penetrative deformation). This event corresponds to the period of development of the carbonate pipes which are interpreted as former fluid conduits comparable to similar structures described in different places (Deville et al., 2006; 2020; De Boever et al., 2006; Nyman et al., 2010; Conti et al., 2014; Zwicker et al., 2015; Tamborrino et al., 2019). This event corresponds also to the period of development of the syn-kinematic calcite veins. We interpret this fracturing and diagenetic stage as related to high fluid pressure at the base of the system (see results of the study of fluid inclusions, Fig. 29) and associated to a sudden and massive flow of fluids from below what is today the decollement level (fluids issued from the carbonates of the Coahuila group). The widespread lack of CL zonation, with only a very faint sector zoning preserved locally, suggests that large calcite crystals have quickly precipitated and are co-genetic (same fluids that have filled the various fractures). This suggests that these fluids have a common origin, the most likely source of calcite being located in the upper part of the Cretaceous carbonates (Coahuila group). The massive precipitation of large calcite crystals in fractures is probably due to the migration of fluids from the carbonates of the Coahuila group (or at least buffered with these carbonates). The isotopic study of calcite veins as shown that $\delta^{18}O$ are very constant in the carbonate rocks of the Coahuila group, in the decollement zone, in the carbonate pipes and in the veins of fractures within the sediments located above the decollement (Fig. 26). This directly suggests that calcite precipitated in similar temperature conditions in all these locations and that the precipitation of the calcite veins above the decollement did not happenedin thermal equilibrium with the host rocks (similar temperature conditions whatever is their structural position and higher temperature conditions compared to cataclasites; e.g. hydrothermal-type fluids; Figs. 26, 27, 28). Considering the syn-kinematic characters of the calcite precipitations at the decollement level, these fluids have obviously circulated at the base of the deltaic system, at the beginning of the decollement processes. It is thus considered that the beginning of the compressive decollement tectonics in shale was marked by a widespread fracturing process (hydraulic fractures) at the base of the deltaic system and at the top of the underlying carbonates, which is consistent with the high overpressure conditions (Figs. 29, 30) deduced from the fluid inclusion study and the burial estimate deduced from field observation (Fig. 6B) and from the backstripping approach (Fig. 28A). Overpressure rise is related to conjugated effects of fluid retention within the shale-rich environment and pressure generation mainly related to clay dehydration and smectite to illite transformation coupled with hydrocarbon gas generation. These fracturing processes were probably the consequence of a major tectonic thickening in the innermost areas (south of the Parras Basin and Sierra Madre). The tectonic thickening was probably at the origin of the development of overpressure in the outer areas, at the deformation front and the increase of pressure has been high enough to generate natural hydraulic fracturing processes. The consequence of this episode of fracturing was an important flow of fluids from the Cretaceous carbonates of the Coahuila group located below the decollement level. Calcite precipitations associated with this flow of dissolved carbonate-rich fluids were found mostly at the base of the deltaic system (upper part of the Parras shale formation and Cerro del Pueblo formation). These fluids have circulated widely at least at the beginning of the decollement tectonics. According to microthermometric results and modeling, these fluids have circulated rapidly since these hot fluids were not in thermal equilibrium with their host rocks during in the precipitation of carbonates in the fractures, as confirmed by the modeled burial history. It is also important to note that some areas (including the decollement zone) were also associated with hydrocarbon migration during this episode of fluid migration. The decollement propagated upward in the stratigraphic series toward the tectonic front.

Stage D: Development of cataclasites. The generation of the cataclasites corresponds to a mechanical damage of the previously precipitated calcite cements associated with faulting. Subsequent to the precipitation of calcite in the fractures, these cements have been tectonically damaged, partly crushed. This process has generated locally cataclasite breccias including polygenic elements. This event was associated with the recrystallization of calcite cements, as indicated by significantly higher $\delta^{18}O$ values than those measured in calcite spars. These values directly suggest lower temperatures of recrystallization than those of the crystalline calcite (see above). If we assume that the recrystallization took place in a closed environment, without the contribution of renewed external fluids, and that the only fluids available were issued from local pressure-solution during cataclasis, recrystallization temperatures can be estimated using a classical fractionation diagram (Fig. 27). The $\delta^{18}O$ of the calcite spars and the T_h measured in fluid inclusions constrain the range of the isotopic compositions of the parent fluids for these calcites between +7‰ and +13‰ (Fig. 27), which is a typical range for basinal evolved fluids. Cataclastic deformations within residual trapped fluids of these compositions, and/or within fluids issued from local pressure-solution associated to these deformation processes at crystal/crystal boundaries (or crystal fragment boundaries), may thus indicate that cataclasite could have formed in a temperature range of 110°C to 160°C (Fig. 27). It is likely that these lower temperatures correspond to those of the host rocks that correspond to the local geothermal conditions at this time (Fig. 28).

Stage E: Hydraulic closure of the thrust system. While early syn-kinematic diagenetic events show evidence of fluid migration from below the decollement level, late syn-kinematic diagenetic events are characterized mainly by quartz precipitation. It can be considered that during the evolution of decollement tectonics, the system tended to be isolated from the influence of dissolved carbonate-rich fluids from depth (from below the decollement zone) and only silica-rich fluids were responsible for the diagenetic processes. We interpret this diagenetic stage as reflecting a form of closure of the system and that silica results from local fluid circulation only issued from either sandstone or clays located above the decollement. The common localization of these silica cements at the periphery of claystone host fragments suggests most probably that clay-rich material is at the origin of quartz precipitation probably during smectite-illite transformation processes (Fig. 21). Indeed, during burial, with the increase of temperature, smectite is transformed into illite with the incorporation of K, sometimes Al, and the release of silica, diverse ions (Na^{2+}, Ca^{2+}, Mg^{2+}, $Fe^{2+/3+}$, ...) and water. Finally, at the end of the period of decollement tectonics, the system located above the decollement level was most probably isolated from fluid migration from below the decollement (closed system). This late stage of thrust tectonics was also characterized by the thermal peak corresponding to the maximum burial. It was also marked by the development of cleavage bands which have favored clay transformations inducing coupled processes between deformation and clay diagenesis.

6. Discussion about shale mobility

The tectonic evolution of this case study can be compared with mechanical experiments made on shale rocks. Increasing importance of shale of deep hydrocarbon exploration targets but also gas/oil shale plays exploration led to improve the knowledge about the rheological properties of shale at depth. Series of geomechanical experiments have shown that, in absence of significant overpressure, the strength of shale rocks increases with depth before reaching the transition from brittle to ductile behavior which appears at relatively moderate depth compared to sandstone and carbonate (Nygard et al., 2006; Jaeger et al., 2007; Fjaer et al., 2008; Strozyk and Tankiewiccz, 2014; Gale et al., 2014; Ge et al., 2015; Holt et al., 2015). The lower is the sandstone fraction in shale, the more ductile the shale (Wang et al., 2015; Labani and Rezaee, 2015). The transition between brittle and ductile is gradual. Notably, Rybacki et al. (2015; 2016) and Yuan et al. (2017) have shown that the brittle-ductile transition in shale occurs currently at a depth between 4 and 5 km. Indeed, critical confining stress of brittle-ductile transition has been estimated to be above 70 MPa (Yuan et al., 2017). For instance, if we consider an average density of 2.6 g/cm^3 for a shale-rich sedimentary column, this is equivalent to a depth of about 4400 m. Indeed, in natural cases, thick shale-rich tectonic wedges have a visco-elastic behavior below 5 km, as it has been evidenced from the geometrical relaxation after a major earthquake (Peterson et al., 2018). Most of the authors consider that the increase of fluid pressure favour the brittle behaviour of rocks associated with the decrease of effective stress (Hubbert and Willis, 1957; Hubbert and Rubey, 1959; Davis et al., 1983; Dahlen et al., 1984; Day-Stirrat et al., 2010, and many others). Indeed, if geomechanical experiments have demonstrated that normally compacted or moderately over-consolidated shale show ductile response to increasing load, on the other side, it has been shown that overpressure build-up turn shale into over-consolidated material which show brittle behavior during loading (Nygard et al., 2006; Yuan et al., 2017). Shale tectonic processes observed during this study are consistent with these later mechanical experiments. In the case study presented here, it has been shown that after a brittle behavior during sedimentation (stage A, characterized notably by fractures injected by sand), an early phase of compressive deformation was characterized by ductile deformation of shale in the lower parts of the tectonic wedge (stage B, Figs. 29, 30). This ductile deformation of shale predated high overpressure conditions during which, finally, brittle deformation prevailed during the overpressure peak (stage C, Figs. 29, 30). The estimated depth where early ductile deformation was prevailing is around 5 km (Fig. 28), which is equivalent to what was obtained in mechanical experimental results (Yuan et al., 2017). The domain of ductile deformation of shale is within the domain of illization of smectite and hydrocarbon gas generation (thermal cracking of organic matter in the gas window; Fig. 28). Concerning the propagation of the decollement, it has long been shown that a decollement corresponds to an interface with a low coefficient of friction between two fragile levels along which displacement can be initiated by excess fluid pressure (Hubbert and Rubey, 1959). In compressive domains with high differential stress, when the fluid pressure excess is high, it is able to produce rupture associated with shearing (Grauls, 1999) which makes possible the activity of a decollement. This is indeed what has been observed in this case study where it has been characterized that the decollement was mostly active during the maximum overpressure period (Figs. 29, 30). With a significant excess of pressure, the stresses tend, over geological times, to be carried gradually by both the solid but also by the fluid inducing a tendency towards a stress-fluid pressure coupling (Tingay et al., 2003) and fractures occur when high pressure excess overtakes the minimum stress plus tension strenght. This is indeed the type of conditions observed at the decollement level in the case studied where the shale sediments, after being deformed ductily, have been affected by fractures injected with fluids, associated with massive calcite precipitation (Figs. 10, 16). The study of fluid inclusions coupled with modeling has shown that the decollement zone at that time reached hydrofracturing pressure conditions (Figs. 28, 29). Similarly, below the decollement, notably in the carbonates of the Coahuila arch, rocks show evidence of massive fracturing processes generating open fractures which have been cemented by single phase calcite cement (Fig. 9B). These processes are interpreted as a result of hydraulic fracturing which is perfectly consistent with the results of the fluid inclusion study and modeling showing that the fracturing processes below the decollement and the decollement activity associated with the massive calcite precipitation event occurred in the required conditions for hydraulic fracturing (Figs. 28, 29).

It was also shown that, although shale behaves locally in a ductile way, no evidence for piercing ductile shale was encountered through the overlying stratigraphic layers (as it is common in salt tectonics). Also, no evidence for liquefaction has been found, except the development of few sedimentary dikes in the innermost part of the study area corresponding to sand mobilization associated with migration of early fluids. During compressive deformation, sedimentary mobilization was only observed as cataclasite injection in fault planes (stage D). From the results of this study, the absence of massive liquefaction process demonstrates that shale tectonics clearly differs from mud volcanism processes which are a consequence of a reaction chain of fluid migration and not a direct mobilization of shale from depth (Deville, 2009; Deville et al., 2010).

7. Conclusion

The area studied is a rare outcropping terrestrial analogue illustrating deformation processes which occur at depth, in thick sedimentary thrust wedges associated with major decollement situated in overpressured shale. It offers outcropping conditions over large areas which made possible a series of different observations and analytical approaches which have shown notably the following points: Massive volumes of deformed shale with scaly fabric, disrupted stratification and boudinage of the sandstone beds are present close to the decollement and in the core of the larger folds. This process of deformation occurred only in the deepest parts of the thrust wedge (below a depth of about 5 km) in the domain of transformation of smectite into illite and hydrocarbon gas generation. The structure of these shale-rich bodies result from very penetrative, distributed deformation (ductile mode of deformation). We interpret these deformed shale-rich sediments as outcropping analogs of deformed sedimentary bodies described as mobile shale at depth on many seismic data all other the world. The deformation mechanisms in these mobile shale-rich units evolved over time from penetrative deformation (scaly fabric and cleavage) to localized brittle deformation (faulting) but the deformation mechanism evolved also laterally in the same formation depending probably on the pressure conditions. As such, both temporal and spatial evolution of the rheology of shale was deduced from our observation. More generally, these results suggest that it is possible to define an ephemeral window where shale is prone to behave in a ductile way below the shale brittle-ductile transition (depth of about 4-5 km) and above high overpressure reaching processes of hydraulic-driven rupture. The brittle deformation was interpreted from the fluid inclusion study as associated to high overpressure close to hydraulic fracturing condition. Also, it is worth noting that the beginning of the decollement tectonics was associated with a percolation of fluids from below the decollement and this process was progressively blocked during deformation without influence from fluid issued from below the decollement (evolution from an open system to a closed system).

Acknowledgements

Thanks are due to TOTAL SA (DBR project) for financial support. Thanks are also due to Nicole Guihlaumou for her help in the work of Clement Dutranoy concerning the fluid inclusions study and to Emily Albouy, Stéphane Raillard and Nadine Ellouz who took part in field-trips in the Parras Basin. Thanks are also due to Michael Joachimski from the University of Erlangen for carbonate isotopic analyses. We thank also the reviewers for their constructive contributions to improve the form of the initial manuscript.

This paper is dedicated to the memory of Marc Tardy.

References

Angus S., Armstrong B., de Reuck K., 1978. International Thermodynamic Tables of the fluid state: Methane. Pergamon, Oxford.

Bartolini, C., Montana, C., Mickus, K., 1995. Geological structure of the Parras Basin-Sierra Madre Oriental area, north-central Mexico utilizing geophysical data. In: AGU 1995 fall meeting. Eos, Transactions, American Geophysical Union. 76, 46, Suppl., 535-536.

Bartolini, C., Mickus, K., 2001. Tectonic blocks, magmatic arcs, and oceanic terrains, a preliminary interpretation based on gravity, outcrop, and subsurface data, Northeast-central Mexico. The western Gulf of Mexico basin, tectonics, sedimentary basins, and petroleum systems. Bartolini Claudio, ed, Buffler Richard T, ed, Cantu Chapa Abelardo, ed. AAPG Mem. 2001, 75, 29-43.

Beyssac, O., Goffe, B., Chopin, C., Rouzaud, J.-N., 2002. Raman spectra of carbonaceous material in metasediments: a new geothermometer. J. Metamorph. Geol., 20, 859–871. https://DOI:10.1046/j.1525-1314.2002.00408.x

Bowers, T.S., Helgeson, H.C., 1983. Calculation of the thermodynamic and geochemical consequences of nonideal mixing in the system H_2O-CO_2-NaCl on phase relations in geologic systems: Equation of state for H_2O-CO_2-NaCl fluids at high pressures and temperatures. Geochimica et Cosmochimica Acta, 47, 7, 1247-1275. https://doi.org/10.1016/0016-7037(83)90066-2

Bradshaw, B.E., Watkins, J.S., 1994. Growth-fault evolution in offshore Texas. Gulf Coast Association of Geological Societies Transactions, 44, 103–110.

Briggs, S.E., Davies, R.J., Cartwright, J.A., Morganz, R., 2006. Multiple detachment levels and their control on fold styles in the compressional domain of the deepwater west Niger Delta. Basin Research 18, 435–450, https://doi:10.1111/j.1365-2117.2006.00300.x

Brown, K.M., 1990. The nature and hydrologic significance of mud diapirs and diatremes for accretionary systems. Journal of Geophysical Research, 95, 8969-8982.

Bruce, C., 1973, Pressured shale and related sediment deformation: mechanism for development of regional contemporaneous faults. AAPG Bulletin, 57, 878–886.

Cohen, H.A., McClay, K., 1996. Sedimentation and shale tectonics of the northwestern Niger Delta front. Marine and Petroleum Geology, 313–328, https://doi:10.1016/02648172(95)00067-4

Conti, S., Fontana, D., Lucente, C.C., Pini, G.A., 2014. Relationships between seep-carbonates, mud volcanism and basin geometry in the Late Miocene of the northern Apennines of Italy: the Montardone mélange. Int. J. Earth Sci. 103, 281–295. https:// doi.org/10.1007/s00531-013-0928-y

Corredor, F., Shaw, J.H., Bilotti, F., 2005. Structural styles in the deep-water fold and thrust belts of the Niger Delta. AAPG Bulletin, 89, 753–780, https://doi:10.1306/02170504074

Davis, D., Suppe, J., Dahlen, F.A., 1983. The mechanics of fold and thrust belts. Journal of Geophysical Research, 88, 1153-1172.

Dahlen, F.A., Suppe, J., Davis D., 1984. Mechanics of fold-and-thrust belts and accretionary wedges: cohesive Coulomb theory. Journal of Geophysical Research, 89, 10 087-10 101.

Day-Stirrat, R.J., McDonnell, A., Wood, L.J., 2010. Diagenetic and seismic concerns associated with interpretation of deeply buried "mobile shales," in L. Wood, ed., Shale tectonics. AAPG Memoir, 93, 5–27.

De Boever, E., Huysmans, M., Muchez, P., Dimitrov, L., Swennen, R., 2009. Controlling factors on the morphology and spatial distribution of methane-related tubular concretions – case study of an Early Eocene seep system. Mar. Pet. Geol. 26, 1580–1591. https://doi.org/10.1016/j.marpetgeo.2008.11.004.

Deville, É., Battani, A., Griboulard, R., Guerlais, S., Herbin, J.P., Houzay, J.P., Muller, C., Prinzhofer, A., 2003. Mud volcanism origin and processes: New insights from Trinidad and the Barbados Prism. Special publication of the Geological Society (London) on Subsurface Sediment Mobilisation. Van Rensbergen, P., Hillis, R.R., Maltman, A.J., & Morley, C.K. (eds), 216, p. 475-490. https://doi:10.1.1.896.2623

Deville, É., Guerlais, S-H., Callec, Y., Lallemant, S, Noble, M., Schmitz, J. and the CARAMBA research team, 2006. Liquefied vs. stratified subsurface sediment mobilization processes: insight from the south of the barbados accretionary prism. Tectonophysics, 428, 33-47. https://doi.org/10.1016/j.tecto.2006.08.011

Deville É., 2009. Mud volcano systems. Nova Publishers, Volcanoes: Formation, Eruptions and Modelling, Chapter 6. Neil Lewis and Antonio Moretti (eds), Nova Science Pub. Inc., 95-126.

Deville É., Guerlais S-H., Lallemant S., Schneider F., 2010. Fluid dynamics and subsurface sediment mobilization processes: An overview from the south-eastern Caribbean. Basin Research, Special issue on fluid flows and Subsurface Sediment Remobilization, 22, 361–379, https://doi.org/10.1111/j.1365-2117.2010.00474.x

Deville É., Scalabrin, C., Jouet, G., Cattaneo, A., Battani, A., Noirez, S., Vermesse, H., Olu, K., Corbari, L., Boulard, M., Marsset, T, Dall'asta, M., Torelli, M, Pastor, L., Pierre, D., Loubrieu, B., 2020. Fluid seepage associated with slope destabilization along the Zambezi Margin (Mozambique). Marine Geology 428, 106275. https://doi.org/10.1016/j.margeo.2020.106275

Eberth, D.A., Delgado-de Jesus, C.R., Lerbekmo, J.F., Brinkman, D.B., Rodriguez de la Rosa, R.A., Sampson, S.D., 2004. Cerro del Pueblo Fm (Difunta Group, Upper Cretaceous), Parras Basin, southern Coahuila, Mexico: reference sections, age and correlation. Revista Mexicana de Ciencia Geologicas 21, 2, 335-352.

Elsley, G.R., Tieman, H., 2010. A comparison of prestack depth and prestack time imaging of the Paktoa complex, Canadian Beaufort MacKenzie Basin, in L. Wood, ed., Shale tectonics. AAPG Memoir 93, 79–90.

Fisher, J.R., 1976. The volumetric properties of H_2O. A graphical portrayal. J. Res. Us Geol. survey, 4, 189-193.

Fjaer, E., Holt, R.M., Horsrud, P., Raaen, A.M., Risnes, R., 2008. Petroleum related rock mechanics, 2nd ed. Elsevier, Amsterdam, 491 p.

Gale, J.F.W., Laubach, S.E., Olson, J.E., 2014. Natural fractures in shale: a review and new observations. AAPG Bull. 98, 11, 2165–216. https://doi:10.1306/08121413151

Ge, H, Yang, L, Shen, Y, Wu, S., 2015. Experimental investigation of shale imbibition capacity and the factors influencing loss of hydraulic fracturing fluids. Pet. Sci. 12, 4, 636–650. https://doi:10.1007/s12182-015-0049-2

Goldstein, R.H., 2001. Fluid inclusions in sedimentary and diagenetic systems. Lithos 55, p. 159-193. https://doi.org/10.1016/S0024-4937(00)00044-X

Grauls, D., 1999. Overpressure: causal mechanism, conventional and hydromechanical approaches. Oil Gas Sci. Technol., 54, 667-678. https://doi.org/10.2516/ogst:1999056

Gray, G.G., Pottorf, R.J., Yurewicz, D.A., Mahon, K.I., Pevear, D.R., Chuchla, R.J., 2001. Thermal and chronological record of syn-to post-Laramide burial and exhumation, Sierra Madre Oriental, Mexico. The western Gulf of Mexico basin, tectonics, sedimentary basins, and petroleum systems. Bartolini Claudio, ed, Buffler Richard T, ed, Cantu chapa Abelardo, ed. AAPG Memoir, 75, 159-181.

Hanor, J.S., 1980. Dissolved methane in sedimentary brines: potential effect on the PVT properties of fluid inclusions. Econ. Geol. 75, 603-609.

Holt, RM, Fjær, E, Stenebraten, JF, Ness, O.M., 2015. Brittleness of shales: relevance to borehole collapse and hydraulic fracturing. Journal of Petroleum Science and Engineering 131, 200–209. https://doi:10.1016/j.petrol.2015.04.006

Hooker, J.N., Larson, T.E., Eakin, A., Marrett, R., 2015. Fracturing and fluid flow in a sub-decollement sandstone; or, a leak in the basement. Journal of the Geological Society 172, 4, 428-442. https://DOI:10.1144/jgs2014-128

Hubbert M.K., Willis, D.G., 1957. Mechanics of hydraulic fracturing. Transactions of the American Institute of Mining, Metallurgical, and Petroleum Engineers, 210, 153–68.

Hubbert, M.K., Rubey, W.W., 1959. Role of fluid pressure in mechanics of overthrust faulting: I. Mechanics of fluid-filled porous solids and its application to overthrust faulting. Geological Society of America Bulletin, 70, 115–66.

Huh, S., Watkins, J.S., Bradshaw, B.E., Xi, J., Kasande, R., 1996. Regional structure and stratigraphy of the Texas shelf, Gulf of Mexico. AAPG Bulletin, 80, 1504–1535.

Ifrim, C., Stinnesbeck, W., Espinosa, B., Ventura, J.F. 2015. Upper Campanian (Upper Cretaceous) cephalopods from the Parras Shale near Saucedas, Coahuila, Mexico. Journal of South American Earth Sciences, 64, 229-257.

Jaeger, J.C., Cook, N.G.W., Zimmerman, R.W., 2007. Fundamentals of rock mechanics, 4th ed. Blackwell, Oxford, 468 p.

Labani, M.M., Rezaee, R., 2015. The importance of geochemical parameters and shale composition on rock mechanical properties of gas shale reservoirs: a case study from the Kockatea Shale and Carynginia Formation from the Perth Basin, Western Australia. Rock Mech Rock Eng. 48, 3, 1249–1257. https://doi:10.1007/s00603-014-0617-6

Lafargue, E., Marquis, F., Pillot, D., 1998. Rock-Eval 6 applications in hydrocarbon exploration, production, and soil contamination studies. Revue de l'Institut Français du Pétrole 53, 4, 421-437.

Lahfid A., Beyssac O., Deville E., Negro F., Chopin C., Goffé B., 2010. Evolution of the Raman spectrum of carbonaceous material in low-grade metasediments of the Glarus Alps (Switzerland). Terra Nova, 22, 354–360. https://doi:10.1111/j.1365-3121.2010.00956.x

Lawton, T.F., Giles, K.A., Vega, F.J., Rosales, D.C., 2001. Stratigraphy and origin of the La Popa Basin, Nuevo Leon and Coahuila, Mexico. The western Gulf of Mexico basin, tectonics, sedimentary basins, and petroleum systems Bartolini Claudio, ed, Buffler Richard T, ed, Cantu chapa Abelardo, ed. AAPG Memoir, 75, 219-240. https://doi.org/10.1306/M75768C9

Lehmann, C., Osleger, D.A., Montañez, I.P., Sliter, W., Arnaud-Vanneau, A., Banner, J. 1999. Evolution of Cupido and Coahuila carbonate platforms, early Cretaceous, northeastern Mexico. GSA Bulletin, 111, 7, 1010-1029.

Lindholm, R.C., Finkelman, R.B., 1972. Calcite staining: semiquantitative determination of ferrous iron. J. Sedim. Petrol. 42, 239-242. https://doi :10.1306/74D724FA-2B21-11D7-8648000102C1865D

Machel, H.G., 2000. Application of cathodoluminescence to carbonate diagenesis. In Pagel M., Barbin V., Blanc P.& Ohnenstetter D., Cathodoluminescence in Geosciences. Springer-Verlag, Berlin, 271-301.

Martínez-Díaz, J.L., Aguillón-Martínez, M.C., Luque, J., Vega, F.J. 2017. Paleocene decapod Crustacea from northeastern Mexico: Additions to biostratigraphy and diversity. Journal of South American Earth Sciences, 74, 67-82.

McBride, E.F., Weidie, A.E., Wolleben, J.A., 1971. Deltaic origin of Difunta group (late Cretaceous to Paleocene), Parras Basin, Coahuila and Nuevo Leon, Mexico. AAPG Bulletin. 55, 2, 352.

McBride, E.F., Wolleben, J.A, Weidie, A.E. 1973. Deltaic and Associated Facies of Difunta Group (Late Cretaceous - Paleocene), Parras and La Popa basins, Coahuila and Nuevo Leon, Mexico. AAPG Bulletin. 57, 9, 1833-1834.

Mc Bride, E.F., Weidie, A.E., Wollenben, J.A., Laudon, R.C., 1974. Stratigraphy and structure of the Parras and La Popa Basins, northeastern Mexico. Geological Society of America Bulletin, 84, 1603-1622.

McBride, E.F., 1974. Significance of color in red, green, purple, olive, brown, and gray beds of Difunta Group, northeastern Mexico. Journal of Sedimentary Petrology. 44, 3, 760-773.

McBride, E.F., Weidie, A.E, Wolleben, J.A., 1975. Deltaic and associated deposits of Difunta Group (late Cretaceous to Paleocene), Parras and La Popa basins, northeastern Mexico. In: Deltas, models for exploration. Broussard Martha Lou (editor). 485-522. Houston Geol. Soc.. Houston, United States.

Morley, C.K., 2003. Mobile shale related deformation in large deltas developed on passive and active margins. Geological Society (London) Special Publication 216, p. 335–357.

Morley, C.K., Guerin, G., 1996. Comparison of gravity driven deformation styles and behavior associated with mobile shales and salt. Tectonics, 15, 1154–1170, https://doi:10.1029/96TC01416

Mullis J. 1979. The system methane-water as a geologic thermometer and barometer from the external part of the central Alps. Bull. Soc. Fr. Minerall. Cristallogr. 102, 526-536.

Murray G.E, Weidie A.E Jr., Boyd D.R, Forde R.H, Lewis P.D Jr. 1962. Formational divisions of Difunta Group, Parras Basin, Coahuila and Nuevo Leon, Mexico. AAPG Bulletin. 46, 3, 374- 383.

Murray, G.E., Boyd, D., Durham, C.O Jr., Forde, R.H, Lawrence, R.M, Lewis, P.D Jr., Martin, K.G, Wolleben, J.A, Weidie, A.E, Wilbert, W.P., 1960. Stratigraphy of Difunta Group, Parras Basin, States of Coahuila and Nuevo Leon, Mexico. Session - International Geological Congress. Part 5, 82-96.

Murray G.E., Boyd D.R., Wilson J.A., Wolleben J.A. 1960. Late Cretaceous fossil locality, eastern Parras Basin, Coahuila, Mexico. Journal of Paleontology. 34, 2, 368-370.

Murray G.E., Wolleben J.A, Boyd D.R. 1959. Difunta strata of Tertiary age, Coahuila, Mexico. 1959. AAPG Bulletin. 43, 10, 2493-2495.

Nyman, S.L., Nelson, C.S., Campbell, K.A., 2010. Miocene tubular concretions in East Coast Basin, New Zealand: Analogue for the subsurface plumbing of cold seeps. Mar. Geol. 272, 319–336. https://doi.org/10.1016/j.margeo.2009.03.021

Nygard, R., Gutierrez, M., Bratli, R.K., Høeg, K., 2006. Brittle–ductile transition, shear failure and leakage in shales and mudrocks. Marine and Petroleum Geology, 23, 201–212. https://doi:10.1016/j.marpetgeo.2005.10.001

O'neil, J.R., Clayton, R.N., Mayeda, T.K., 1969. Oxygen isotope fractionation in divalent metal carbonates. J. Chem. Physics, 51, 5547-5558.

Machel, H.G., 2000. Application of cathodoluminescence to carbonate diagenesis. In Pagel, M., Barbin, V., Blanc, P., Ohnenstetter D., Cathodoluminescence in Geosciences. Springer-Verlag, Berlin, 271-301.

Peterson, K. E., Barnhart, W. D., Li, S. 2018. Viscous accretionary prisms: Viscoelastic relaxation of the Makran accretionary prism following the 2013 Baluchistan, Pakistan earthquake. Journal of Geophysical Research: Solid Earth, 123. https://doi.org/10.1029/2018JB016057.

Rybacki, E., Reinicke, A., Meier, T., Makasi, M., Dresen, G., 2015. What controls the mechanical properties of shale rocks? – Part I: Strength and Young's modulus. Brittleness. Journal of Petroleum Science and Engineering 135, 702–722. https://doi.org/10.1016/j.petrol.2015.10.028

Rybacki, E., Meier, T., Dresen, G., 2016. What controls the mechanical properties of shale rocks? – Part II: Brittleness. Journal of Petroleum Science and Engineering 144, 39–58. http://dx.doi.org/10.1016/j.petrol.2016.02.022

Roedder, E., Bodnar, R.J., 1980. Geological pressure determinations from fluid inclusion studies. Ann. Rev. Earth Planet. Sci. 8, 263-301.

Roedder, E. 1984. Fluid inclusions. Mineralogical Society of America. Rev. Mineralogy, 12, 644 p.

Setzmann, U., Wagner, W., 1991. A new equation of state and tables of thermodynamic properties for methane covering the range from melting line to 625 K at pressures up to 1000 Mpa. J. Phys. Chem. Ref. Data 20, 1061-115.

Shepherd, T., Rankin, A.H., Altderton, D.H.M., 1985. A practical guide to fluid inclusion studies. In Blackie (Ed.), Chapman et Hall. New York, 239 p.

Soegaard, K., Ye, H., Halik, N., Daniels, A.T., Arney, J., Garrick, S., 2003. Stratigraphic evolution of Latest Cretaceous to early Tertiary Difunta foreland basin in northeast Mexico: Influence of salt withdrawal on tectonically induced subsidence by the Sierra Madre Oriental fold and thrust Belt, in C. Bartolini, R.T. Buffler, and J Blickwede, eds., The Circum-Gulf of Mexico and the Caribbean: Hydrocarbon habitats, basin formation, and plate tectonics: AAPG Memoir 79, 364-394.

Strozyk J, Tankiewicz M. The undrained shear strength of overconsolidated clays. Procedia Eng. 91, 317–321. https://doi:10.1016/j.proeng.2014.12.067

Tamborrino, L., Himmler· T., Elvert· M., Conti· S., Gualtieri· A., Fontana· D., Bohrmann· G. 2019. Formation of tubular carbonate conduits at Athina mud volcano, eastern Mediterranean Sea. Marine and Petroleum Geology 107, 20-31. https://doi.org/10.1016/j.marpetgeo.2019.05.003

Tardy, M, Ramirez, R.C, Patino, A.M., 1975. El frente de la napa de Parras (conjunto Cadena Alta-Altiplano central) en el area de Aramberri, N. L., Sierra Madre Oriental, Mexico. Revista -Instituto de Geologia. 2, Universidad Nacional Autonoma de Mexico, Instituto de Geologia. Mexico, D.F., Mexico, 1-11.

Tardy, M., 1980. Contribution a l'étude geologique de la Sierra Madre Oriental du Mexique: Tesis doctoral, Université Pierre et Marie Curie de Paris, 445 p.

Tingay, M., Hillis, R., Morley, C., Swarbrick, R., Okpere, E., 2003. Pore pressure/stress coupling in Brunei Darussalam - implications for shale injection. in P. Van Rensbergen, R. R Hillis, A.J. Maltman & C.K. Morley (eds), Subsurface Sediment Mobilization. 369-379. Geological Society of London. https://10.1144/GSL.SP.2003.216.01.24.

Van Rensbergen, P., Morley, C.K., 2000. 3D seismic study of a shale expulsion syncline at the base of the Champion Delta, offshore Brunei and its implications for the early structural evolution of large delta systems: Marine and Petroleum Geology, v. 17, p. 861–872, doi:10.1016/S02648172(00)00026-X.

Van Rensbergen, O., Hillis, R. R., Maltman, A. J., Morley, C. K., 2003a. Subsurface sediment mobilization: Introduction, in P. Van Rensbergen, R. R. Hillis, A. J. Maltman, and C. K. Morley, eds., Subsurface sediment mobilization: Geological Society (London) Special Publication 216, 1–8.

Van Rensbergen, P., and C. K. Morley, 2003b, Re-evaluation of mobile shale occurrences on seismic sections of the Champion and Baram deltas, offshore Brunei: Geological Society (London) Special Publication, p. 395–409.

Vega, F.J., Ahyong, S.T., Espinosa, B., Flores-Ventura, J., Luna, L., González-González, A.H. 2018. Oldest record of Mathildellidae (Crustacea: Decapoda: Goneplacoidea) associated with Retroplumidae from the Upper Cretaceous of NE Mexico. Journal of South American Earth Sciences 82, 62-75. https://doi.org/10.1016/j.jsames.2017.12.002

Vogt, M., Stinnesbeck, W., Zell, P., Kober, B., Kontny, J., Herzer, N., Frey, E., Rivera-Sylva, H.E., Padilla Gutierrez, J.M., Amezcua, N., Huerta, D.F., 2016. Age and depositional environment of the "dinosaur graveyard" at Las Águilas, southern Coahuila, NE Mexico. Palaeogeography, Palaeoclimatology, Palaeoecology, 441, 758-769. https://doi.org/10.1016/j.palaeo.2015.10.020

Wachter, E., Hayes, J.M., 1985. Exchange of oxygen isotopes in carbon-dioxide - phosphoric acid systems. Chemical Geology 52, 365-374. https://doi.org/10.1016/0168-9622(85)90046-6

Wang, D., Ge, H., Wang, X., 2015. A novel experimental approach for fracability evaluation in tight-gas reservoirs. J. Nat. Gas Sci. Eng. 23, 239–249. https://doi:10.1016/j.jngse.2015.01.039

Warning, K.R, McBride, E.F., 1976. Transgressive-regressive deposits of Difunta Group (upper Cretaceous-Paleocene), Parras Basin, Mexico. AAPG Bulletin 60, 4, AAPG-SEPM annual meeting, 732.

Weidie, A.E. Murray, G.E, Cameron, C.P, Long, J.J. Jr., Ritchie, E.J., 1966. Stratigraphy and structure of Parras Basin and adjacent areas of northeastern Mexico. AAPG Bulletin 50, 3, 639-640.

Weidie, A.E., Murray, G.E., 1967. Geology of Parras Basin and adjacent areas of northeastern Mexico. AAPG Bulletin 51, 5, 678-695.

Weidie, A.E., Wolleben, J.A, McBride, E.F., 1978. Geologic framework of northeastern Mexico. In: Minas de Golondrinas and Minas Rancherias, northeastern Mexico. 27-38.

Wiener, R.W., Mann, M.G., Angelich, M.T., Molyneux, J.B., 2010. Mobile shale in the Niger Delta: Characteristics, structure, and evolution, in Wood, ed., Shale tectonics. AAPG Memoir 93, 145–160.

Wolleben, J.A., 1977. Paleontology of the Difunta Group (Upper Cretaceous-Tertiary) in northern Mexico. Journal of Paleontology 51, 2, 373-398. http://www.jstor.org/stable/1303616

Wood, L., 2010. Shale tectonics: A preface. In L. Wood, ed, Shale tectonics; AAPG Memoir 93, 1-4. https://DOI:10.1306/13231305M93730

Wood, L., 2012. Shale tectonics. In Wood, L., 2012. Shale tectonics. In Phanerozoic Passive Margins, Cratonic Basin and Global tectonic Map. 43-54. https://DOI:10.1016/B978-0-444-56357-6.00002.0

Yuan, Y-S., Jin, Z-J., Zhou, Y., Liu, J-X., Li, S-J., Liu, Q-Y., 2017. Burial depth interval of the shale brittle–ductile transition zone and its implications in shale gas exploration and production. Pet. Sci. 14, 637–647. https://DOI:10.1007/s12182-017-0189-7

Zwicker, J., Smrzka, D., Gier, S., Goedert, J.L., Peckmann, J., 2015. Mineralized conduits are part of the uppermost plumbing system of Oligocene methane-seep deposits, Washington State (USA). Mar. Pet. Geol. 66, 616–630. https://doi.org/10.1016/j. marpetgeo.2015.05.035

FIGURES

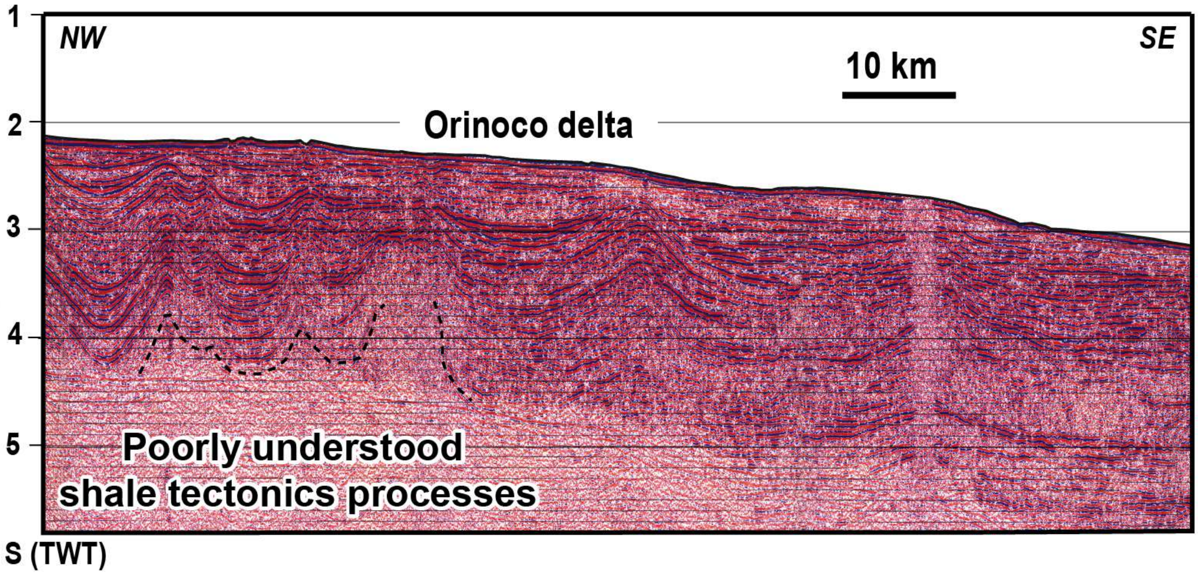

Fig. 1. A typical example of a seismic line from the Orinoco delta – Barbados accretionary prism junction (modified from Deville et al., 2010) showing shale tectonics features at depth, as observed on seismic reflection data in many areas of the world.

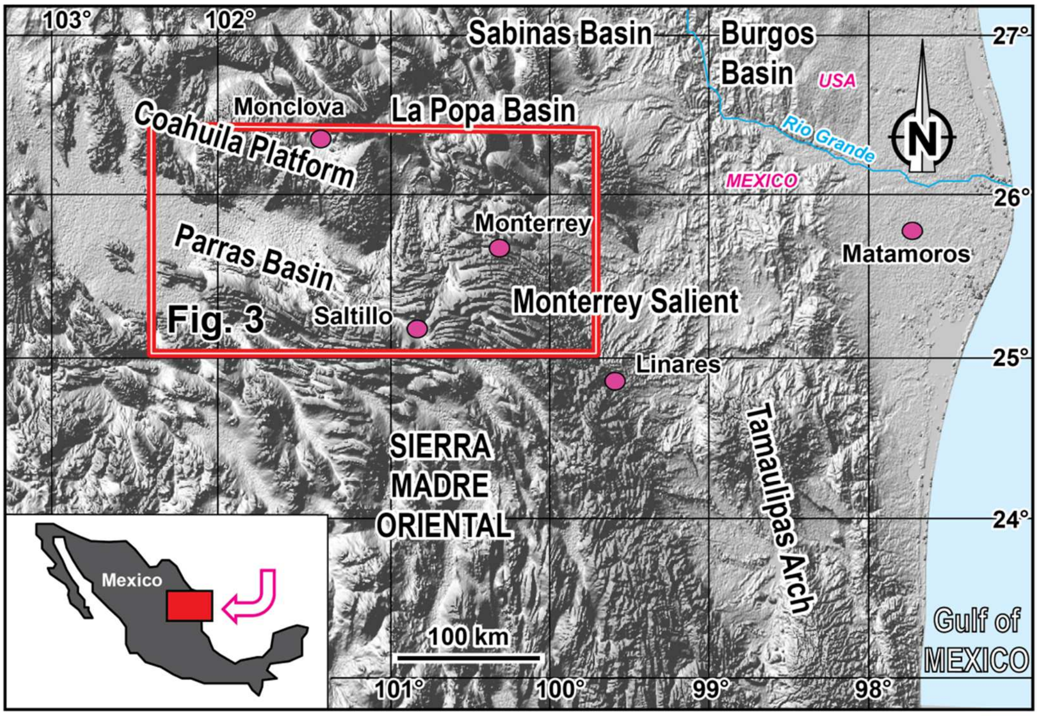

Fig. 2. Location of the study area in north-eastern Mexico (DEM downloaded from https://lpdaacsvc.cr.usgs.gov).

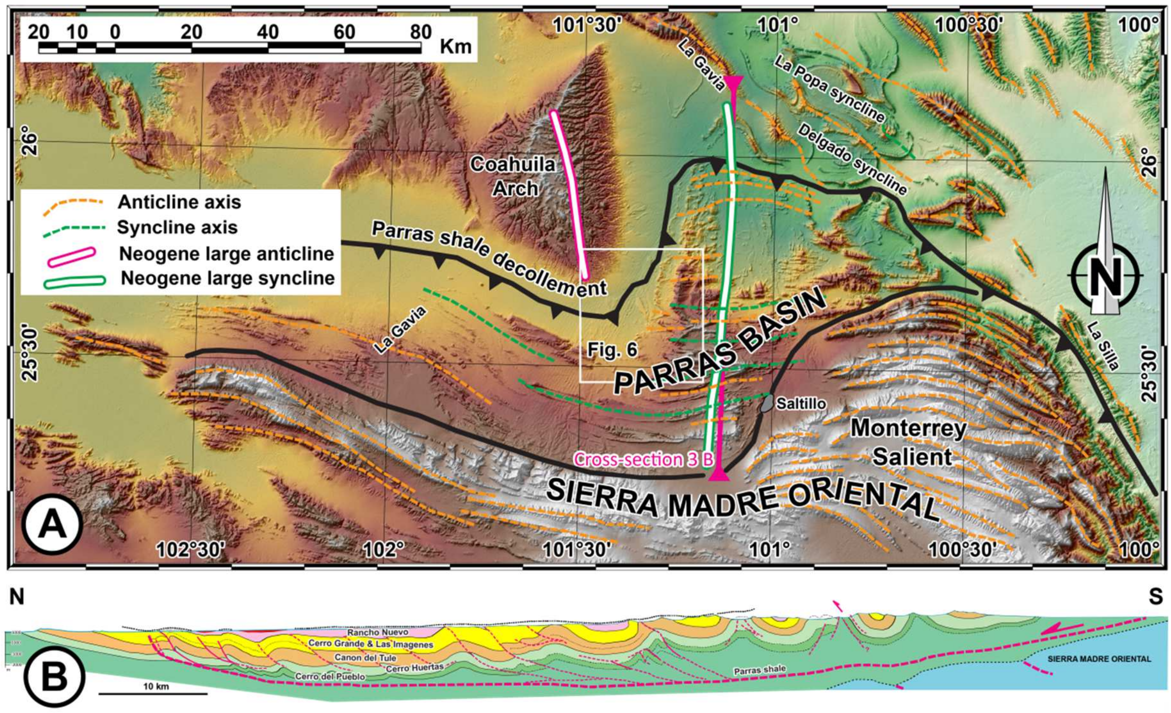

Fig. 3. Structural sketch-map (**A**) and geological section (**B**) of the study area (No vertical exaggeration).

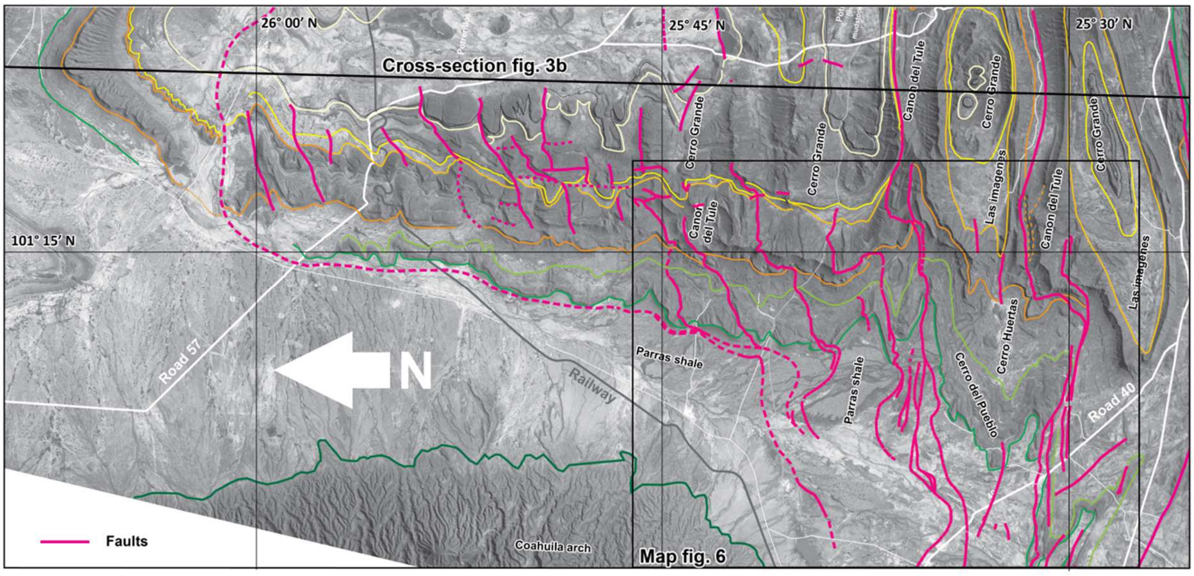

Fig. 4. Satellite image (Lansat) covering the study area. Because of the uplift of the Coahuila Arch to the west and because of the uplift-related erosion of Campanian-Maastrichtian layers, present-day outcrops in this area illustrates directly the structure of the Parras compressive structures (as an initial cross-section before the uplift), allowing direct observations and rock sampling all over the cross-section.

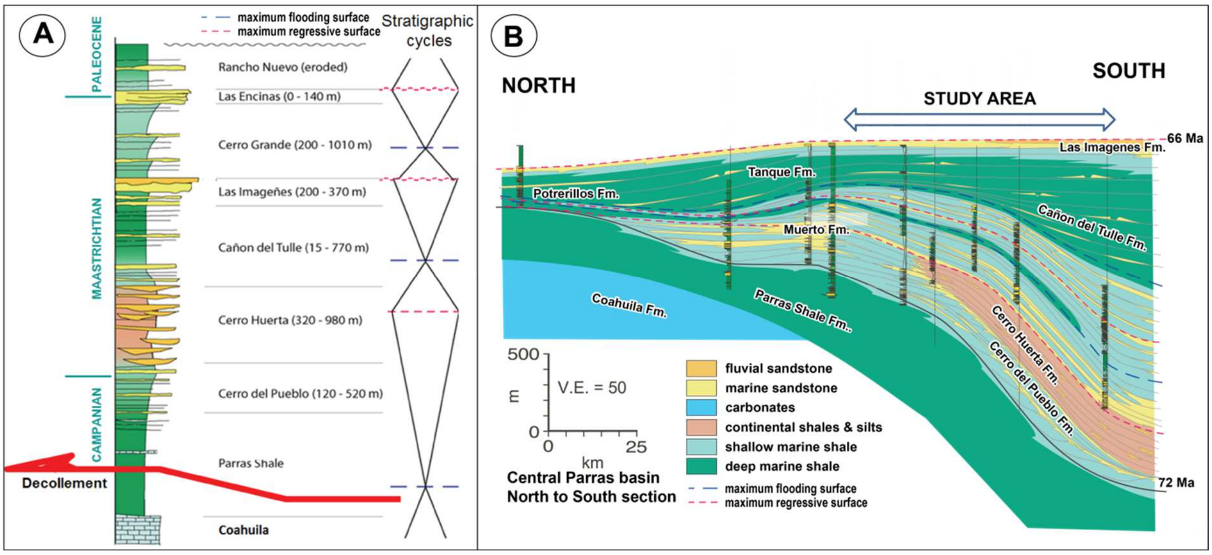

Fig. 5. A. Simplified stratigraphic column of the Parras Basin (not at scale). **B.** Facies correlation of sedimentologic sections in the central Parras Basin (compilation of field works by Soegaard et al., 2003 and this study; detailed stratigraphic logs are from Soegaard et al., 2003).

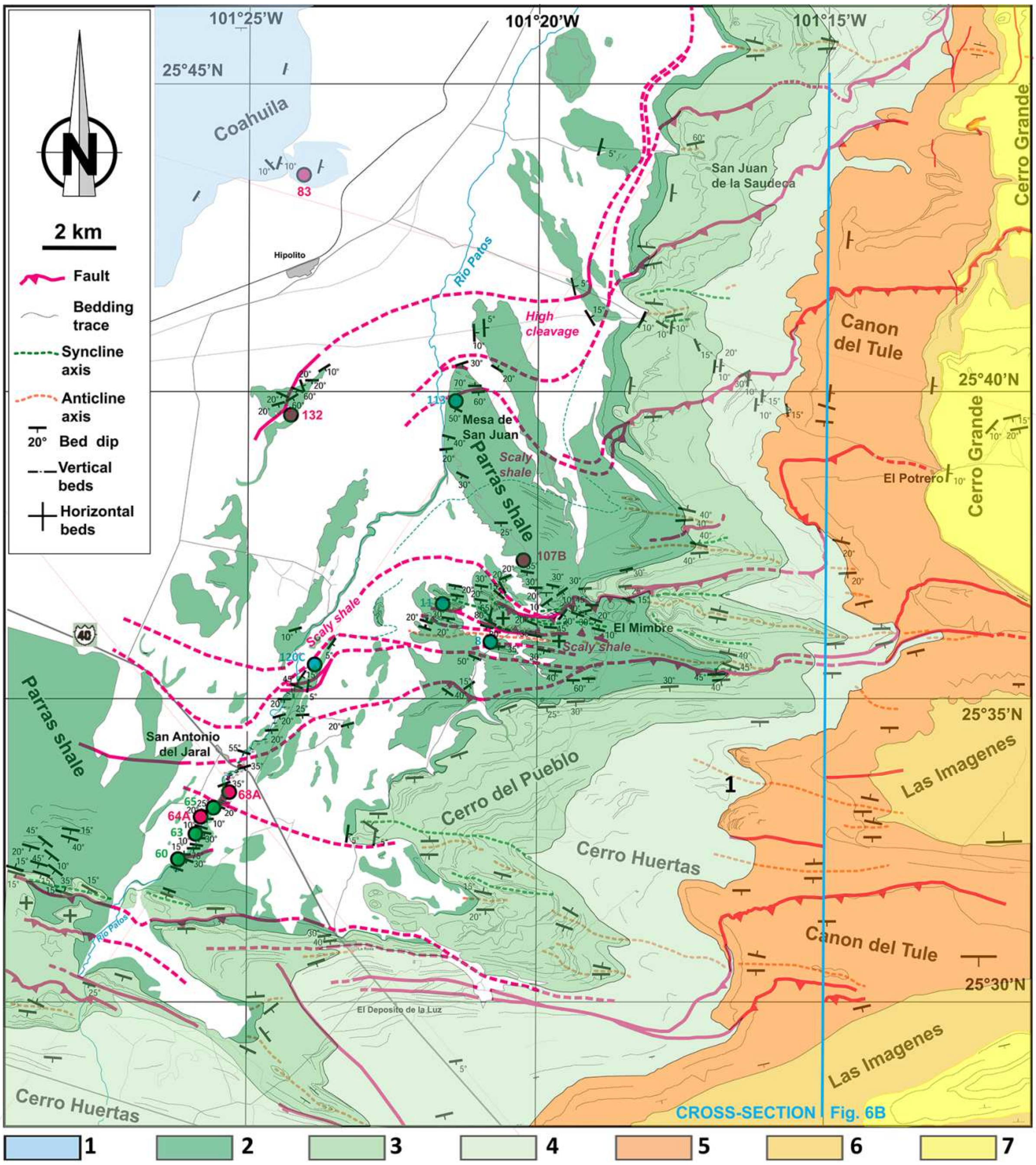

101°25'W
101°20'W
101°15'W
25°45'N
25°40'N
25°35'N
25°30'N
N
2 km
Fault
Bedding trace
Syncline axis
Anticline axis
20° Bed dip
Vertical beds
Horizontal beds
Coahuila
83
Hipolito
Rio Patos
High cleavage
132
113
Mesa de San Juan
Parras shale
Scaly shale
107B
El Mimbre
San Juan de la Saudeca
Canon del Tule
Cerro Grande
El Potrero
Scaly shale
120C
40
San Antonio del Jaral
Parras shale
68A
65
64A
63
60
Cerro del Pueblo
Cerro Huertas
Las Imagenes
El Deposito de la Luz
Cerro Huertas
CROSS-SECTION Fig. 6B
1
2
3
4
5
6
7

A

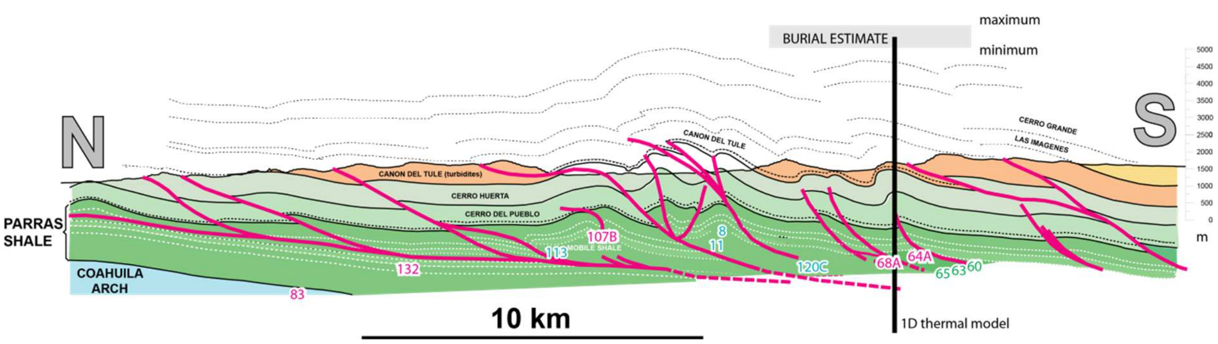

BURIAL ESTIMATE
maximum
minimum
N
S
CANON DEL TULE
CERRO GRANDE
LAS IMAGENES
CANON DEL TULE (turbidites)
CERRO HUERTA
CERRO DEL PUEBLO
PARRAS SHALE
COAHUILA ARCH
MOBILE SHALE
107B
113
132
83
8
11
120C
68A
64A
65
63
60
m
10 km
1D thermal model

B

Fig. 6. A. Geological map in the area of San Antonio del Jaral and Hipolito (Location in Fig. 3); 1. Carbonate of the Coahuila group; 2. Parras shale formation; 3. Cerro de Pueblo formation; 4. Cerro Huertas formation; 5. Canon del Tule formation; 6. Las Imagenes formation; 7. Cerro Grande formation (see ages and description in the text). **B.** Geological cross-section with location of the 1D thermal model presented in Fig. 28.

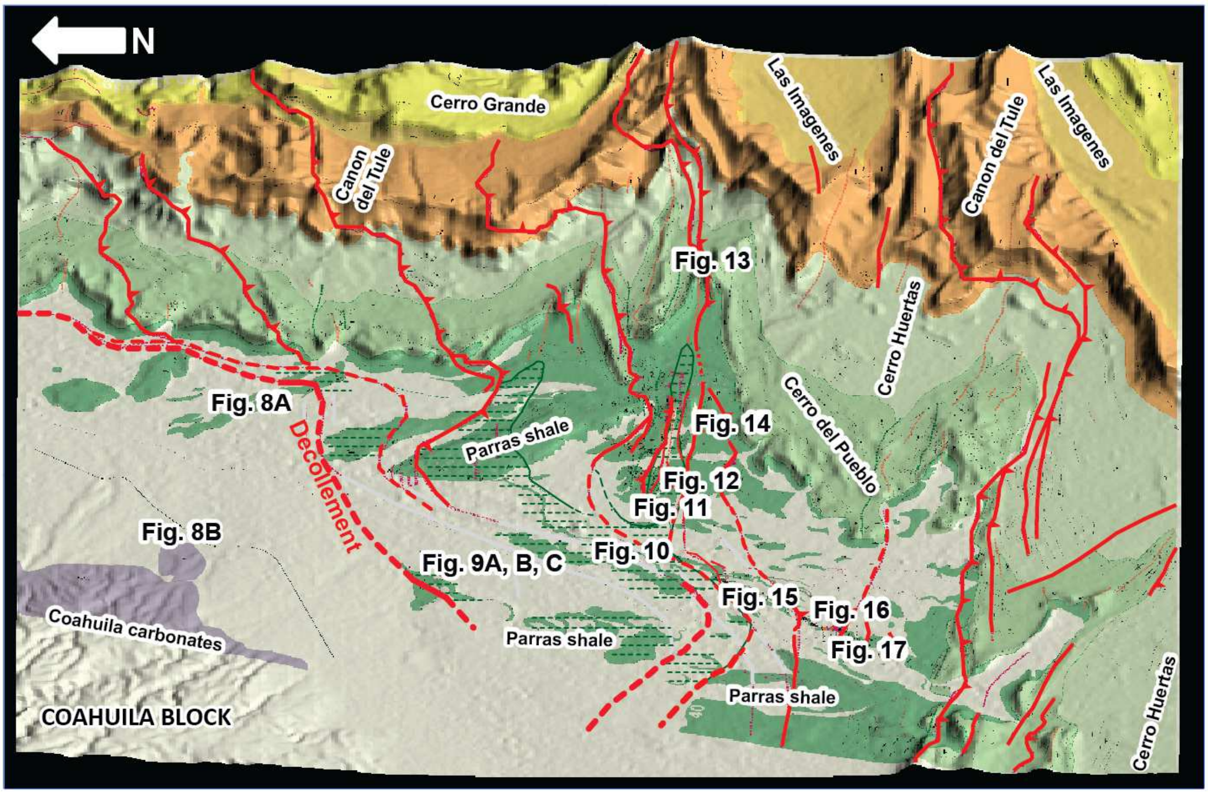

Fig. 7. Structural block diagram with location of the photographs of Figs. 8, 9, 10, 11, 12, 13, 14, 15, 16, and 17. Doted-lines within the Parras shale correspond to scaly shale areas.

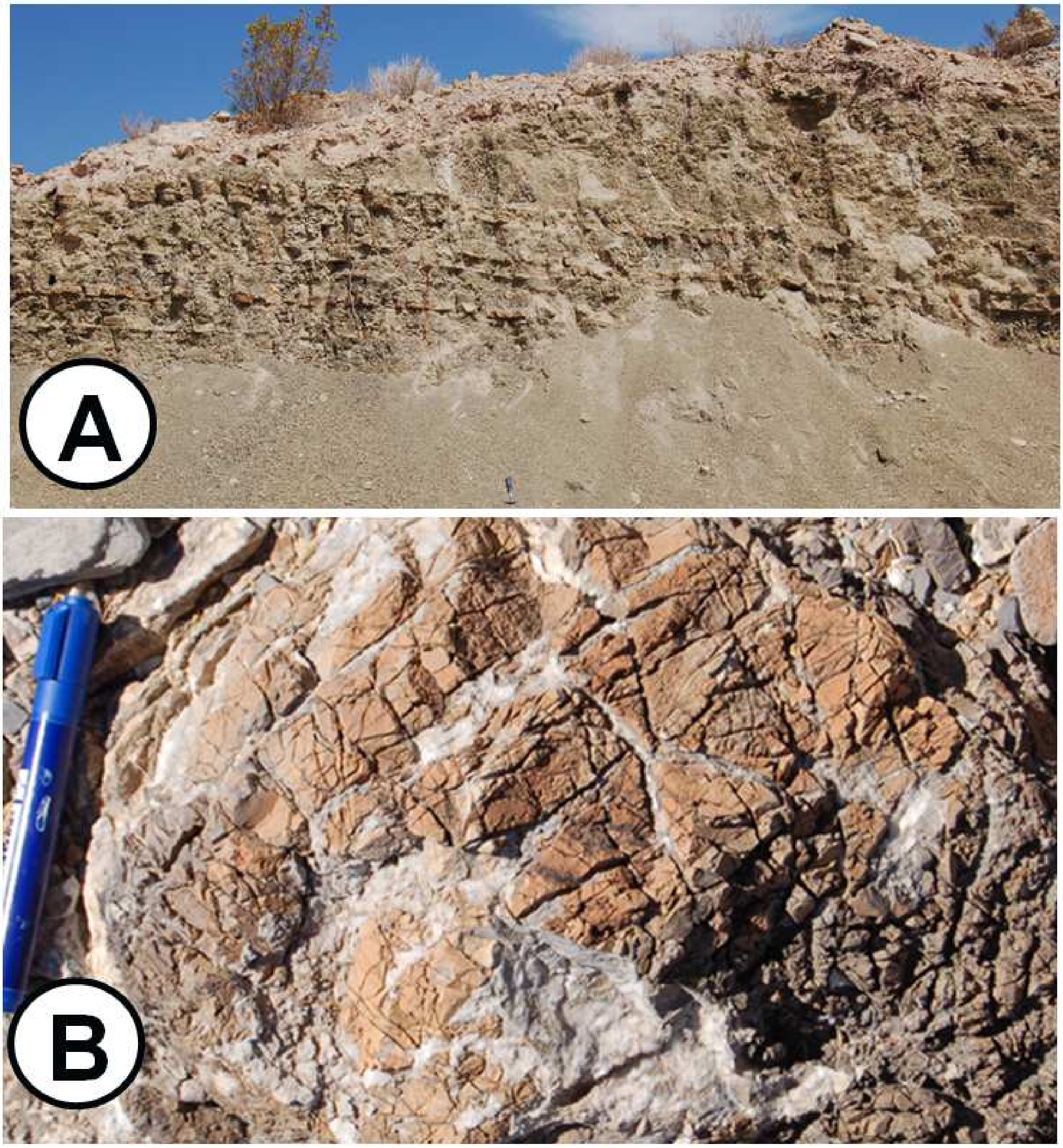

Fig. 8. A. Continuous stratification in the Parras shale located above the Coahuila group and below the basal decollement (location of sample 132 located in Fig. 6A and cross-section 6B). **B.** The breccias observed at the top of the pelagic carbonates of the Coahuila group. These rocks correspond to anisotropic fracturing with mass precipitation of carbonate cements (large calcite crystals) precipitated in a single generation. We interpret these rocks as the result of natural hydraulic fracturing (location sample 83 located in Fig. 6A and cross-section 6B).

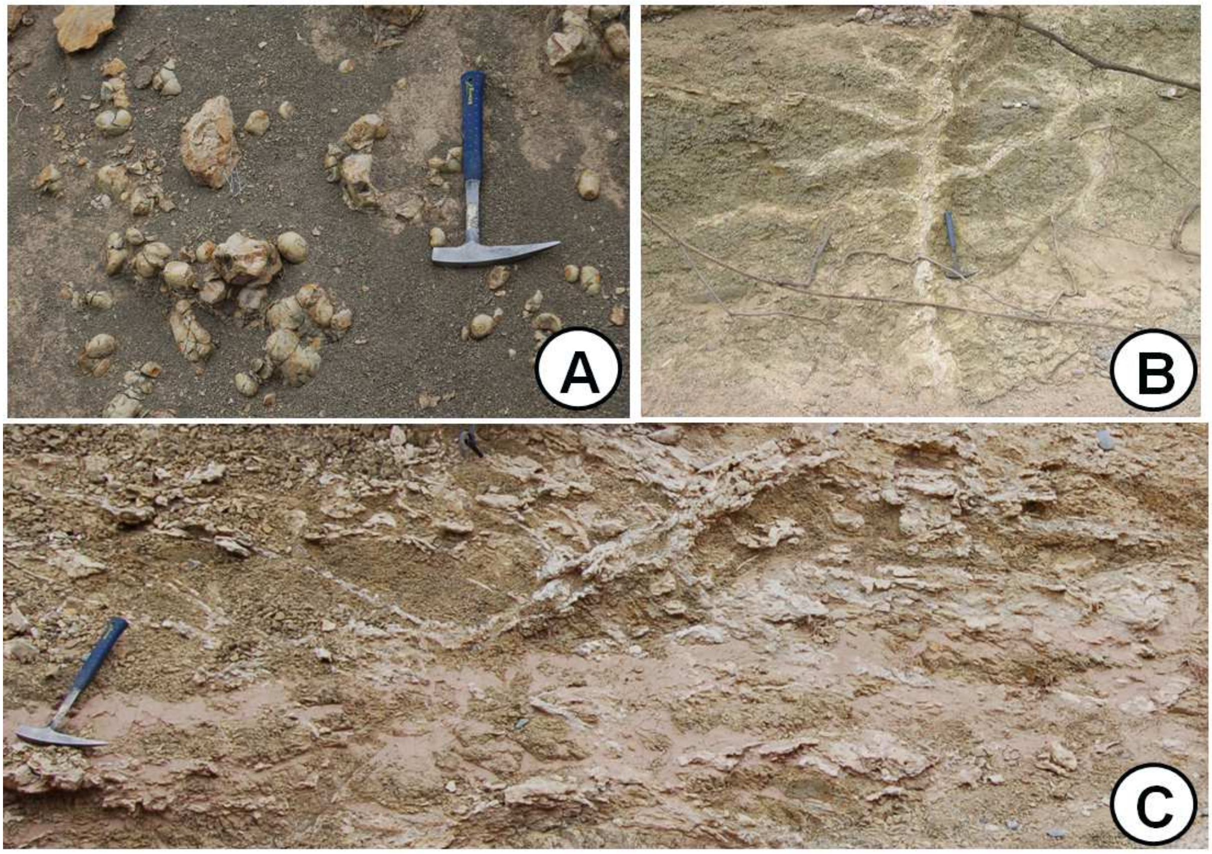

Fig. 9. A. Carbonated concretions in the Parras shale formation located in the decollement area. **B.** Carbonated diffuse zones interpreted as traces of ancient fluid migration pathways within shale above the decollement. **C.** The decollement zone: Scaly fabric shale associated with massive cataclasites and tectonic breccias in the basal decollement.

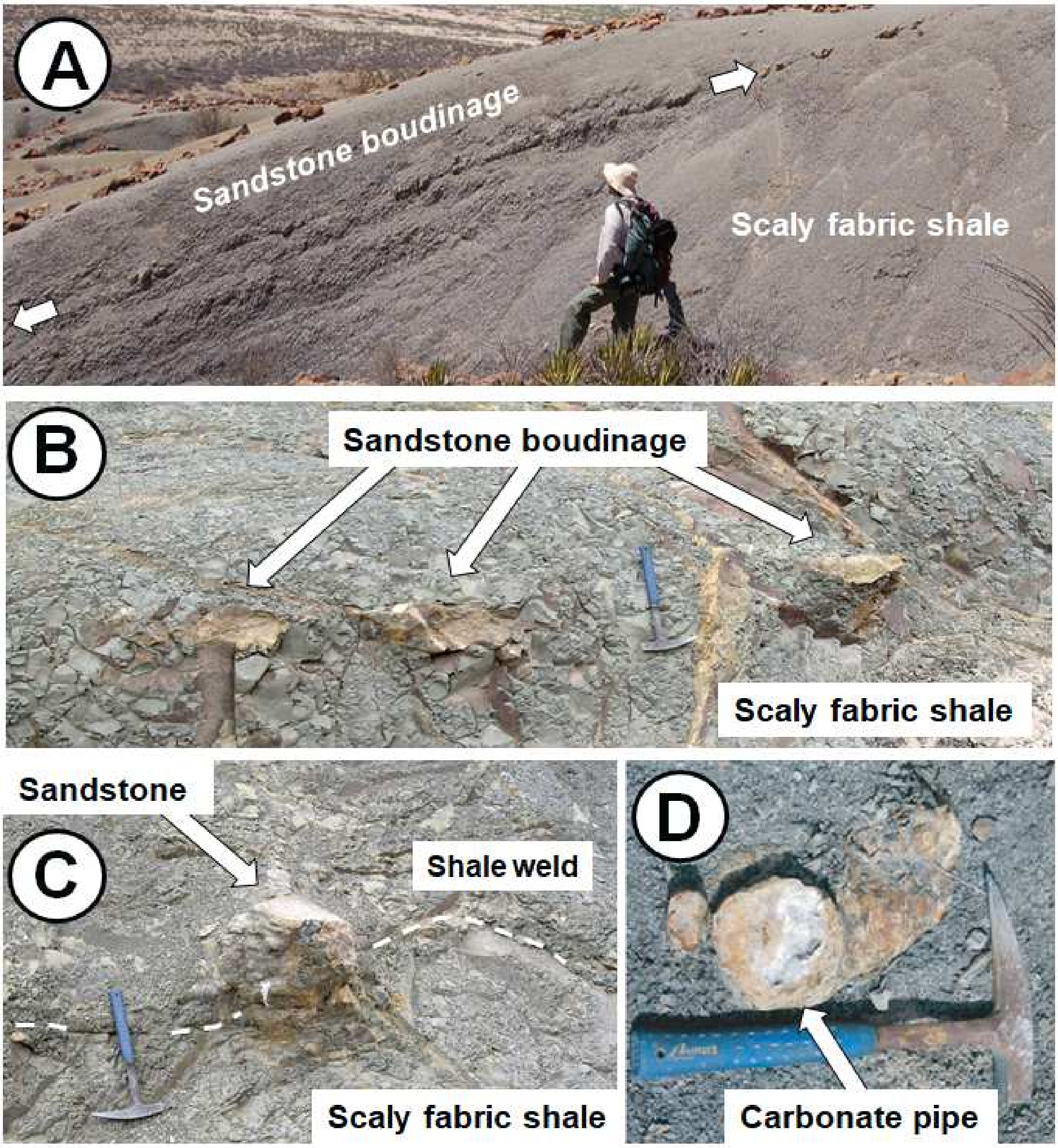

Fig. 10. "Mobile shale": how it looks like on the field in the zone located above the decollement (Campanian Parras shale). **A**. Homogeneous scaly fabric shale with disrupted stratification and intense boudinage of sandstone layers. **B.** and **C.** Isolated boudinated element of sandstone within deformed scaly fabric shale. **D.** Carbonate tube interpreted as a fossil fluid conduit through the scaly fabric shale layers.

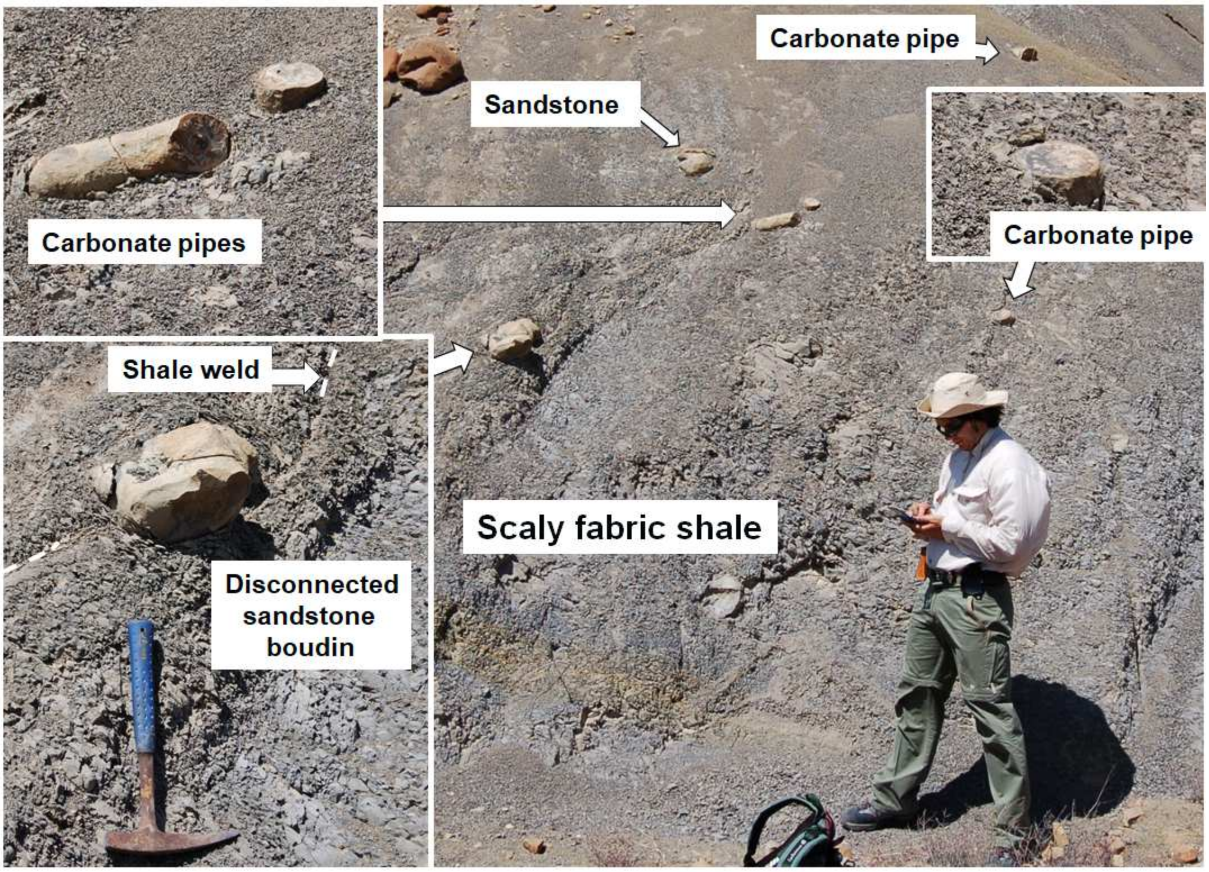

Fig. 11. 'Mobile' scaly fabric shale with sandstone boudins and fluid conduits in the shale-rich cores of the main anticlines.

Fig. 12 - Thrust plane mineralized by carbonate cements cross-cutting the "mobile" scaly fabric shale. This structure is located in the core of a large fold (location in Fig. 7).

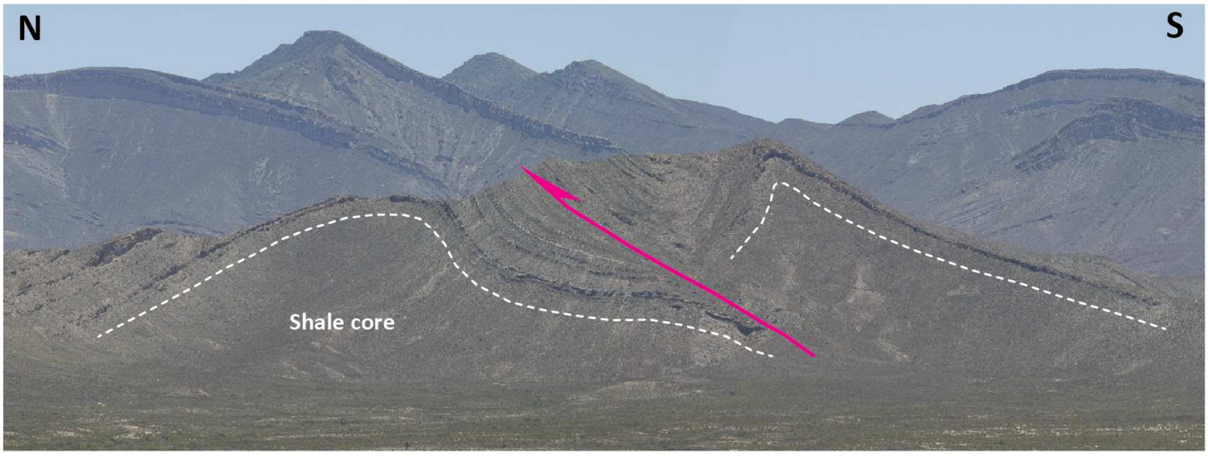

Fig. 13 - Sandstone-rich top of the shale-rich core of large folds. Note that the top of the ‘mobile shale’ of the core of the folds is not intrusive within the upper layers. It is faulted as the upper layers.

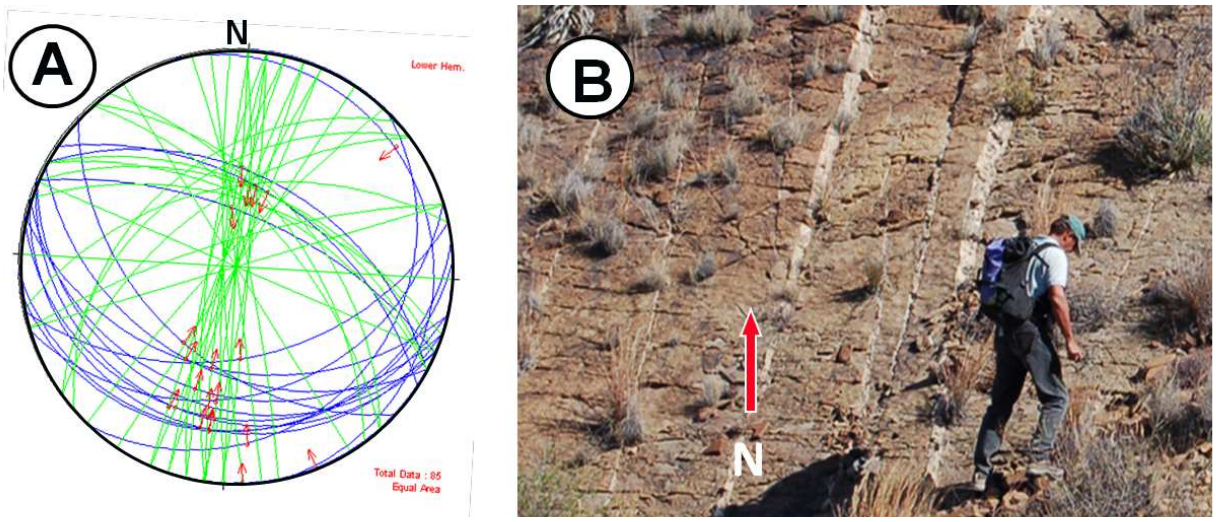

Fig. 14 - Fracturing processes of the sandstone-rich envelop of the limbs of the main folds. **A**. Stereonet of fracture measurements. Note the abundant subvertical fractures trending N15° parallel to the slikenlines of the fault planes (blue: faults, red arrows: slikenlines on fault planes; green: open fractures; projection lower hemisphere equal area; 85 measurements). **B.** Cemented opened fractures trending N15°.

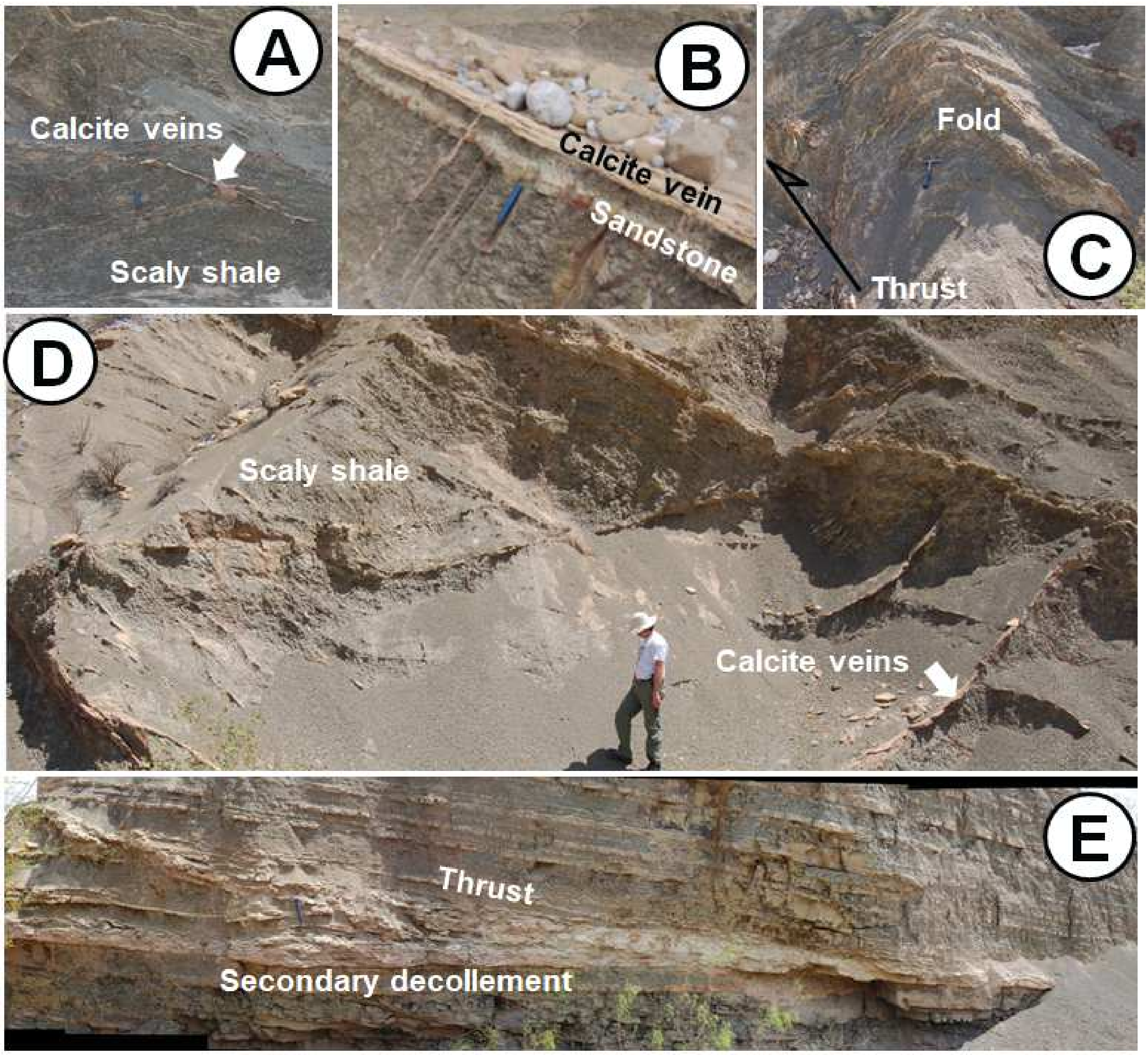

Fig. 15. Deformation processes in the area located above the basal decollement (Location in Fig. 7). **A.** Penetrative cleavage and cross-cutting shear bands with carbonate cements. **B.** An example of low angle fault (characterized by the precipitation of calcite) located few centimeters above a thin sandstone layer. Such features are common in the study area. **C.** A minor fold above a thrust plane**. D.** Penetrative cleavage zone with shear bands mineralized by carbonate cements. **E.** A secondary decollement with the initiation of a thrust.

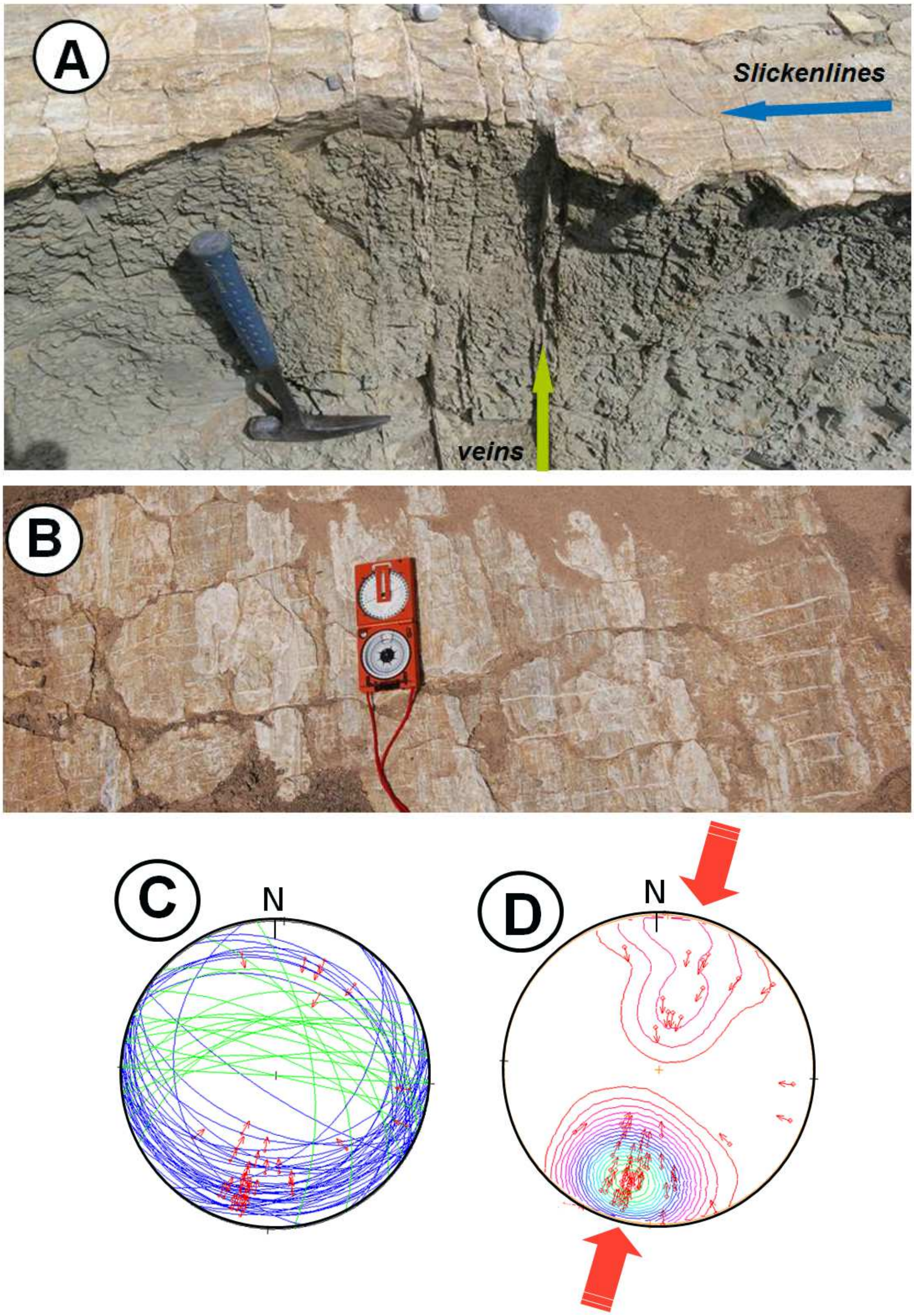

Fig. 16. A. Photo illustrating fracturing processes in and around the decollement zone. **B.** open fractures perpendicular to the slickenlines (late re-fracturing of striated calcite planes in the fault planes interpreted as the result of a late N-S extension process). **C.** Stereonet of fractures in the lower part of the thrust wedge (blue: faults, red arrows: slickenlines on fault planes; green: open fractures; projection lower hemisphere equal area; 70 measurements). (**D**) Cumulative stereonet (projection lower hemisphere equal area; 116 measurements) of slickenlines on fault planes (preferential orientation N15°).

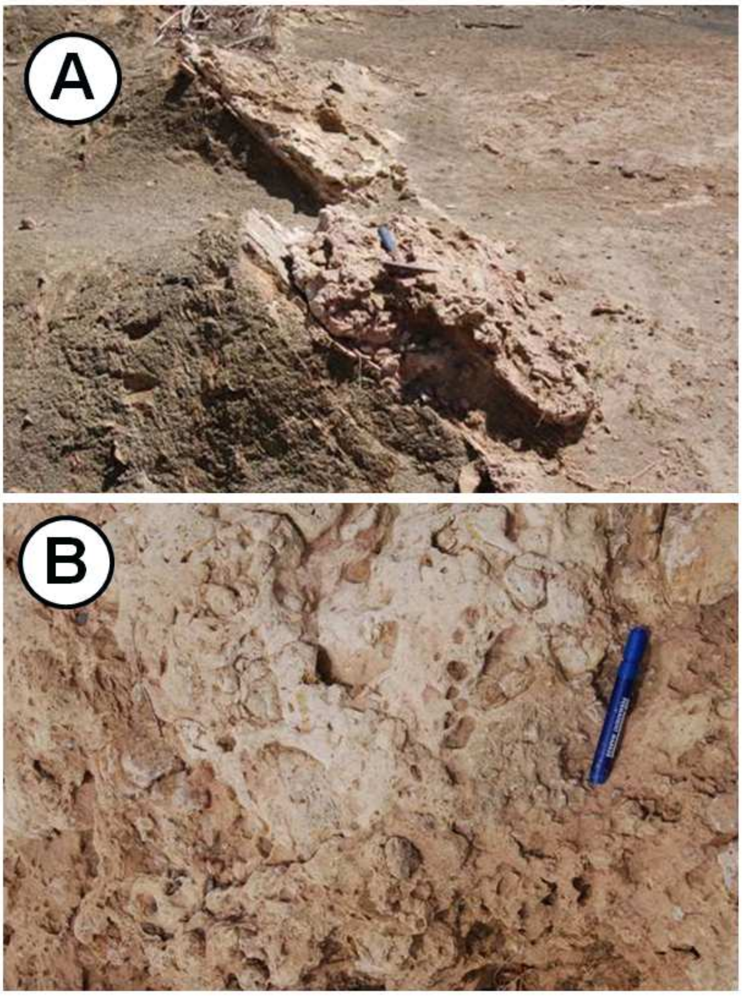

Fig. 17. Example of lenses of cataclasite (**A**) and fault breccia including polymitic clasts (**B**).

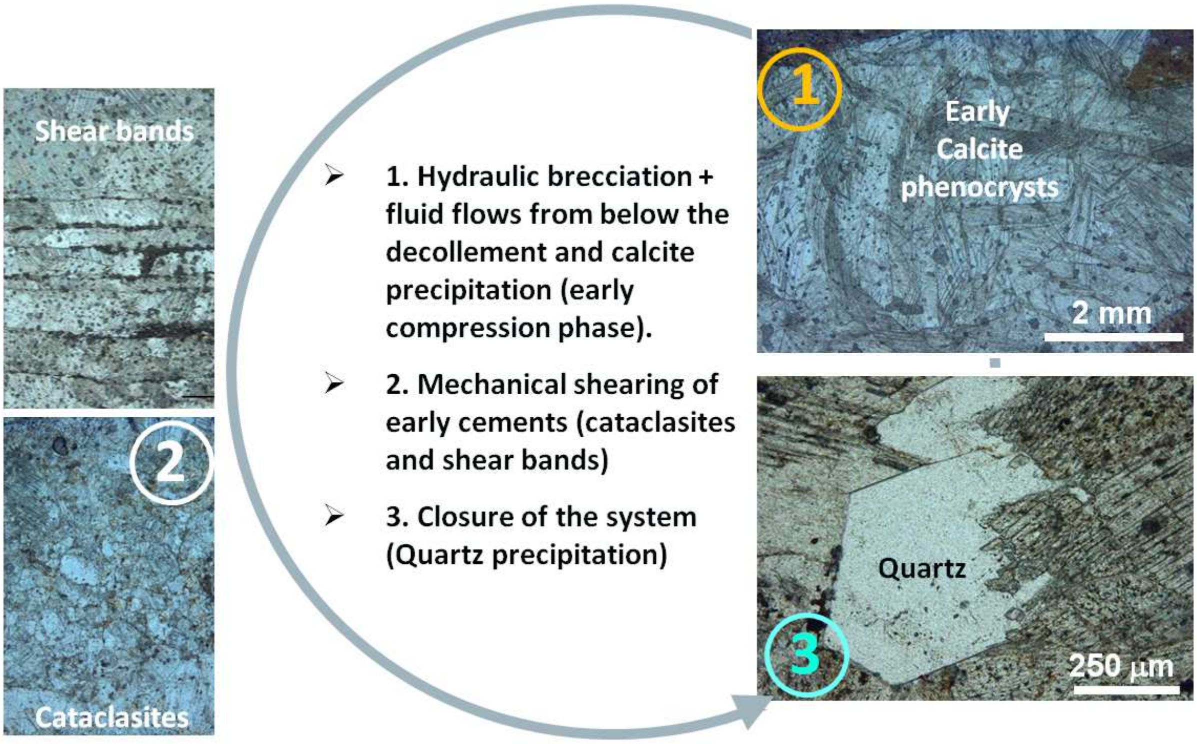

Fig. 18. The three main syn-kinematic diagenetic stages: 1. Calcite precipitation, 2. Cataclasites and shear bands development, 3. Quartz precipitation.

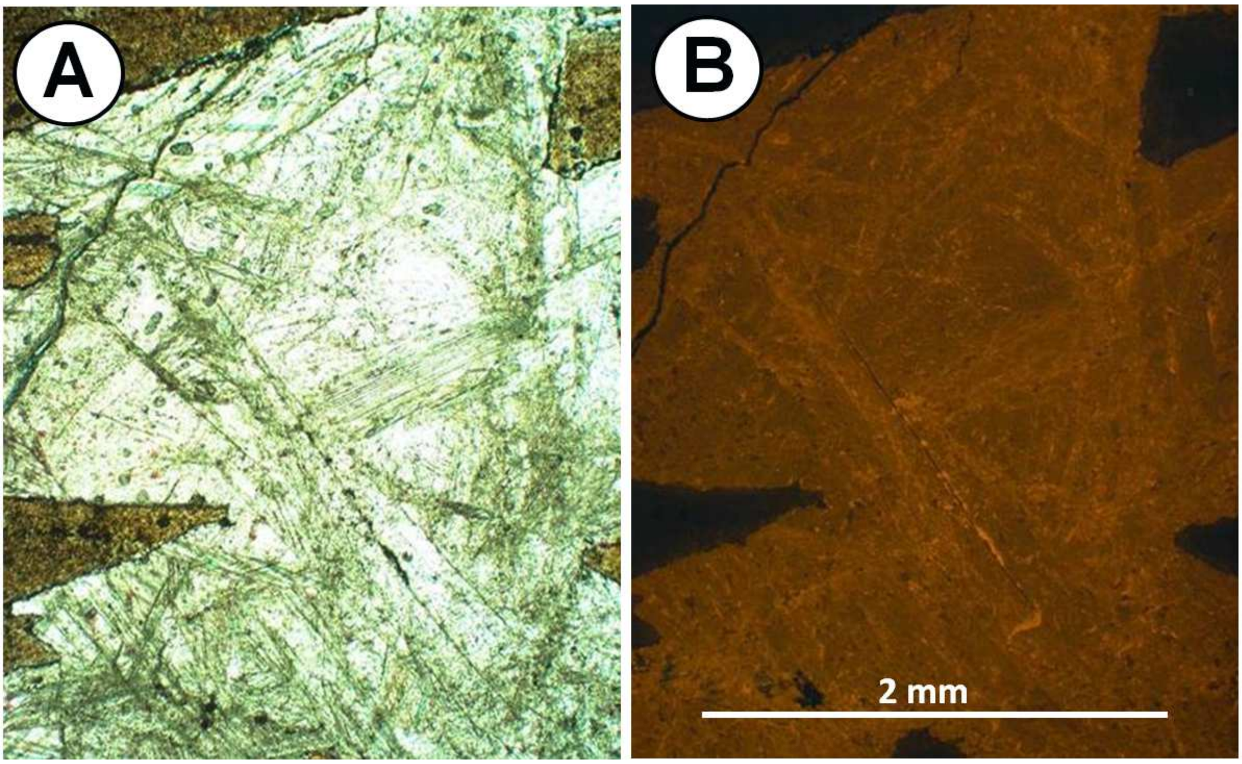

Fig. 19. Large calcite crystals. Comparison of plane polarized light (**A**) and CL (**B**) of the calcite cement (note the homogeneous dull brown luminescence).

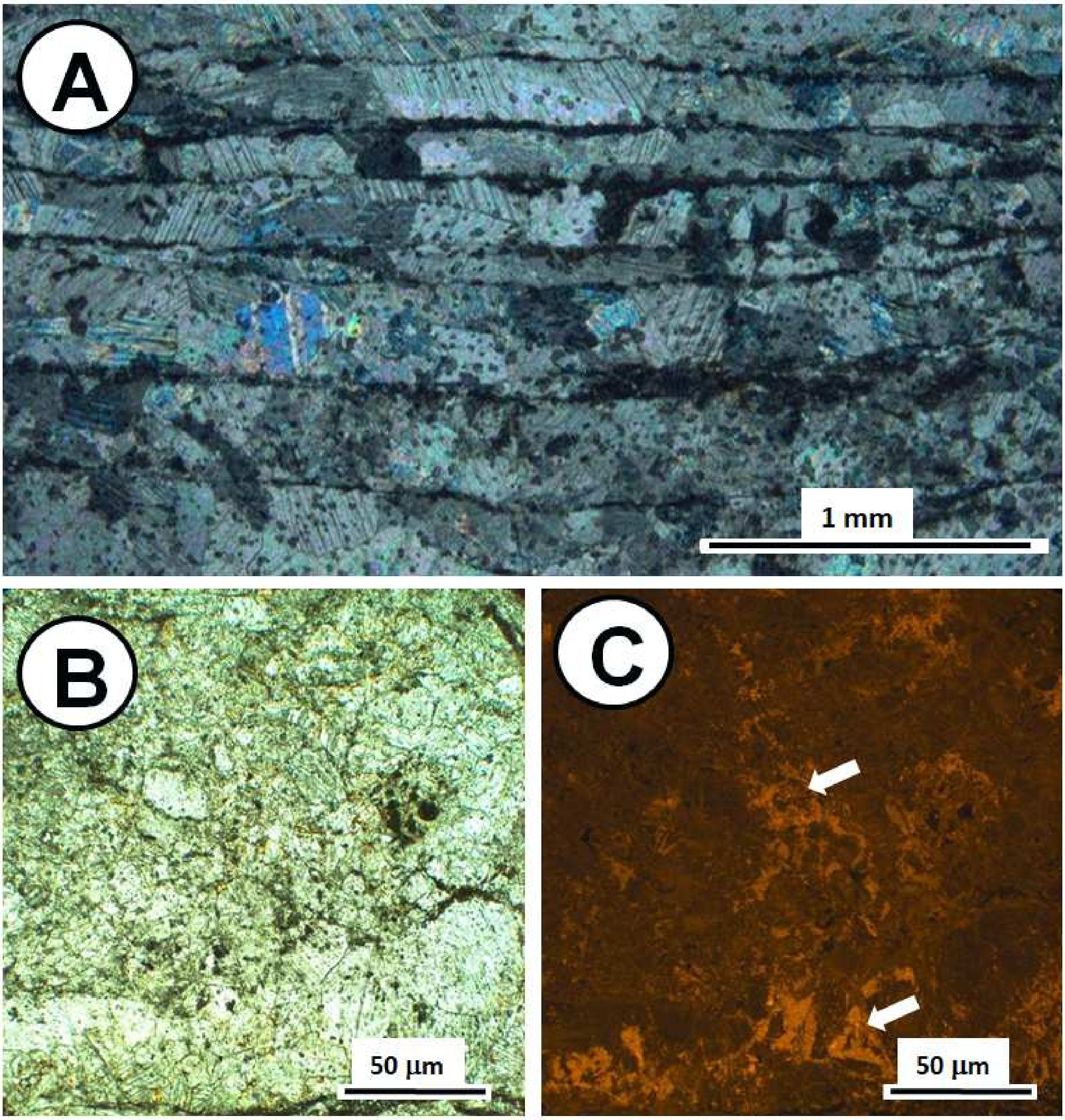

Fig. 20. Destruction of early cements. Sheared early calcite cements (**A**) and crushed early calcite cements (cataclasites) compared in transmitted light (**B**) and CL (**C**); note the presence of faint sector zoning in the less crushed calcite crystals (arrows).

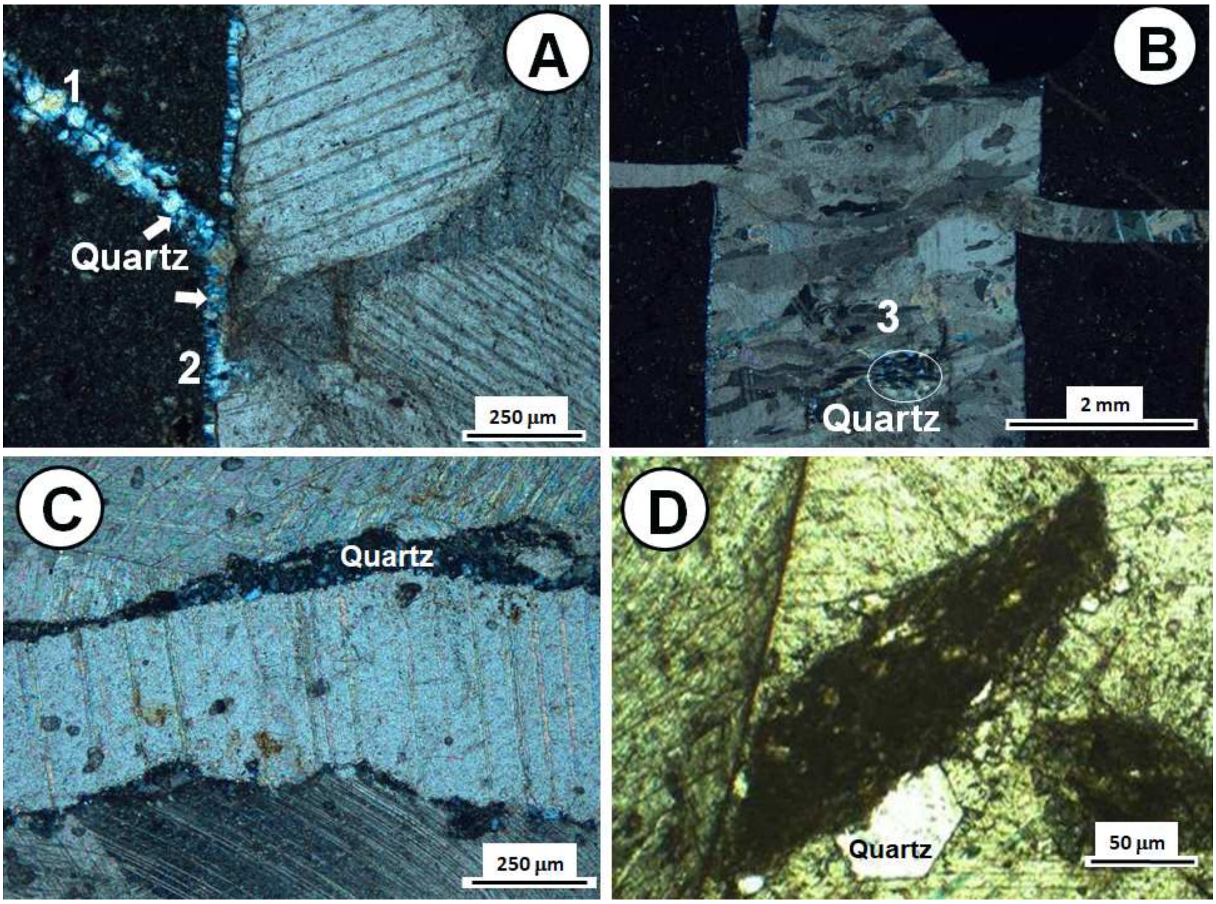

Fig. 21. Quartz precitations. **A** and **B**: Two photographs of thin section (cross-polarized light) illustrating late quartz precipitation in rocks sampled below the basal decollement, either (1) as newly-formed veins, or (2) on the side of previous calcite veins (**A**), or else (3) in the core of sparitic calcite veins (**B**). **C:** Syn-kinematic late quartz veins in rocks sampled above the basal decollement (polarized light). **D:** Precipitation of quartz at the periphery of claystone clasts (host) (plane polarized light).

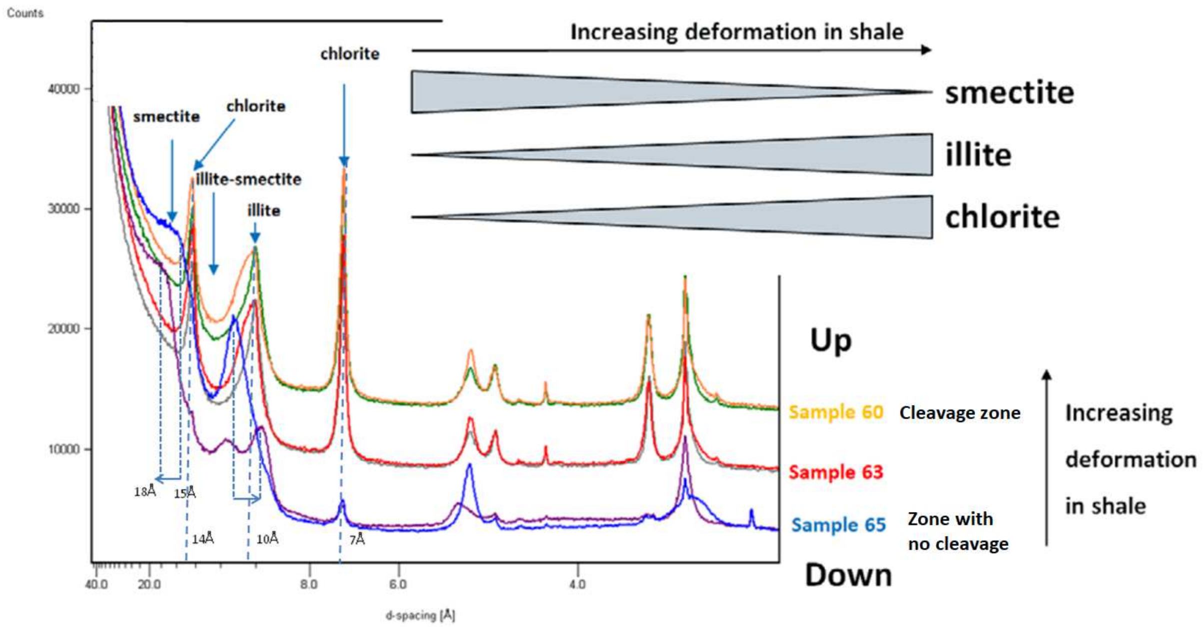

Fig. 22. XRD analysis results showing gradient of illitization in the cleavage zones showing the influence of the deformation on the mineralogical transformation of clays (see explanation in the text; sample location in Fig. 6A).

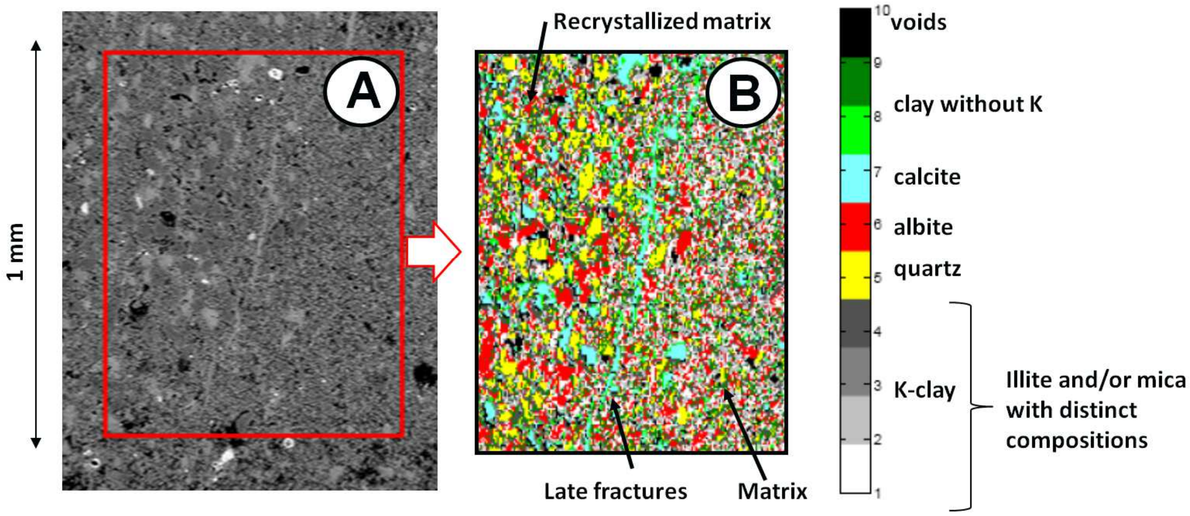

Fig. 23. The structure and transformation of clay minerals in scaly shale characterized by scanning electronic microprobe (A. SEM textural view; B. SEM mineralogical mapping; sample from outcrop shown in Fig. 15D; location in Fig. 7)

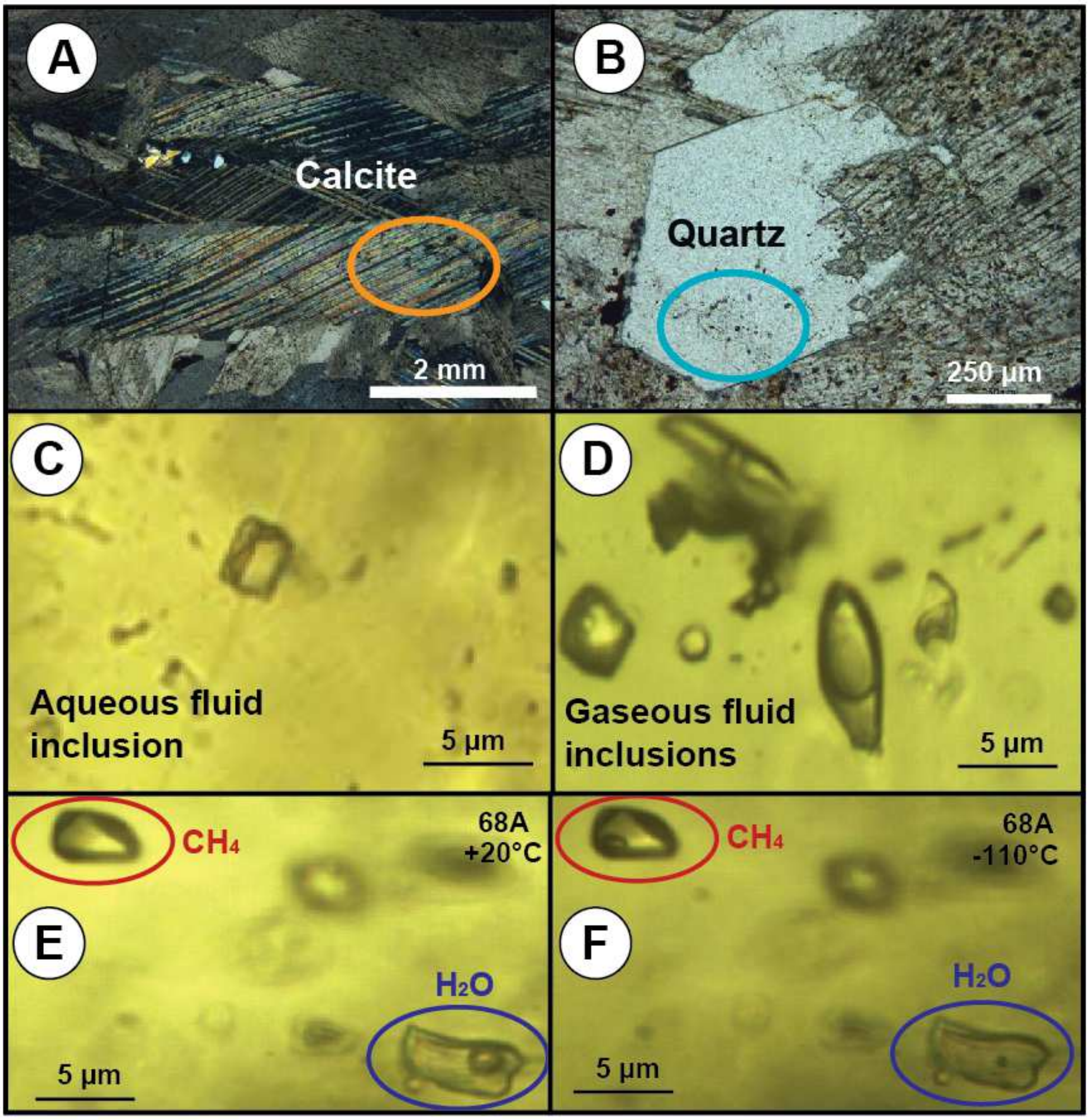

Fig. 24. Characteristic fluid inclusions (sample 68A; location in Fig. 6A): Fluid inclusions in calcite (**A**.) and in quartz (**B**.), circled areas correspond to zones of high density of fluid inclusions; **C**. Aqueous fluid inclusions in calcite; **D**. Gaseous fluid inclusions in calcite. Cogenetic CH_4-dominant and H_2O-dominant fluid inclusions observed in calcite at 20°C (**E**) et -110°C (**F**).

Mineral	Structural context	Sample	Tfm (°C)	Tmi (°C)	Th (°C)	Est. burial (km)	Correction (°C)	T trapping (°C)
Calcite	Shale-rich fold core	107B	-49	-0.5	130	5	25	155
	Top decollement zone	64A	-53	-0.5	160	5.4	-	160
	Upper decollement zone	68A	-51	-1	170	5.5	-	170
	Decollement sole thrust	132	-49	0	170	6	30	200
	Top Coahuila carbonates	83	-	-0.5	180	7	35	215
Quartz	Top decollement zone	64A	-	0	215		-	215
	Upper decollement zone	68A	-	0	220		-	220

Table 1. Melting temperatures and estimated trapping temperatures of aqueous fluid inclusions (samples location in Fig. 6A). T_{fm} : first melting temperature of ice; T_{mi} : final melting temperature of ice; T_h : homogenization temperature; Est. burial: estimated burial as shown in Fig. 6B; temperature corrections were made in fluid inclusions with no presence of methane; T trapping: temperature of trapping of the fluid inclusions.

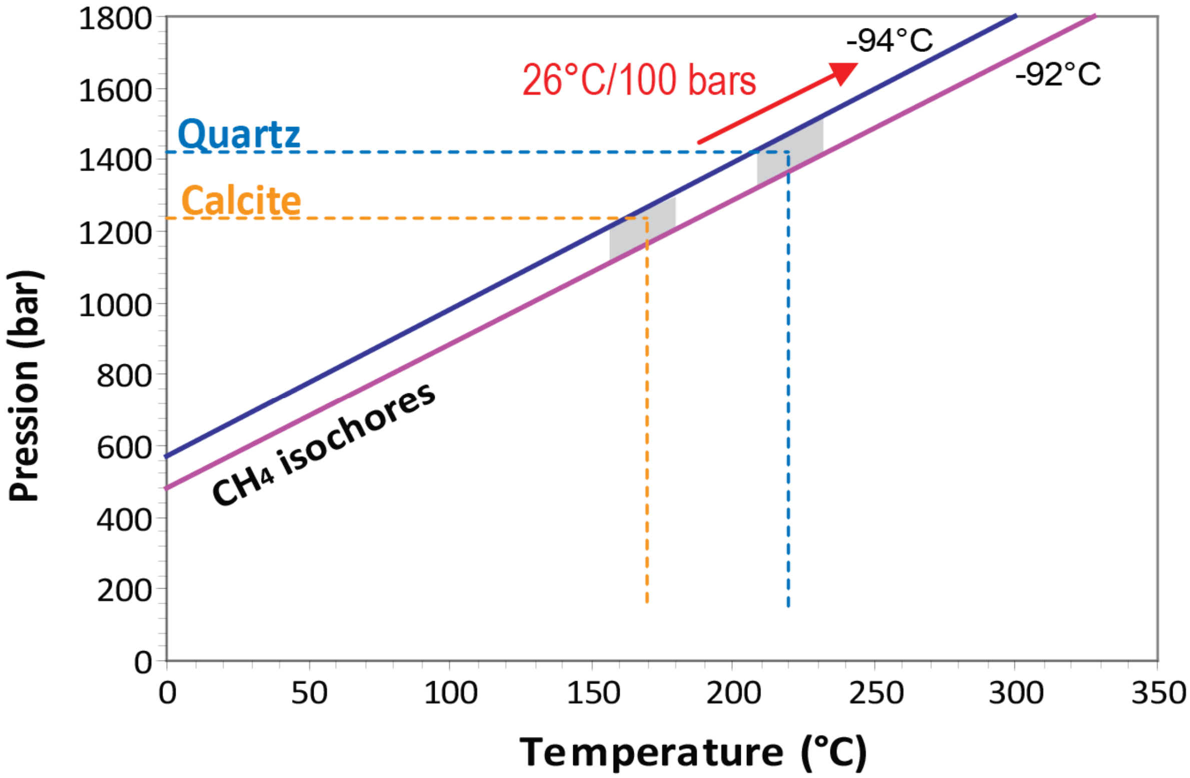

Fig. 25. Trapping pressure and temperature of aqueous fluid inclusions which are saturated with dissolved methane of sample 68A (location in Fig. 6A). In this case, the measured T_h are equivalent to the trapping temperatures. Methane isochores from Setzmann and Wagner (1991). Calcite: T=165-170°C; P= 1240±40 bars, quartz: T=225-230°C; P= 1430±50 bars.

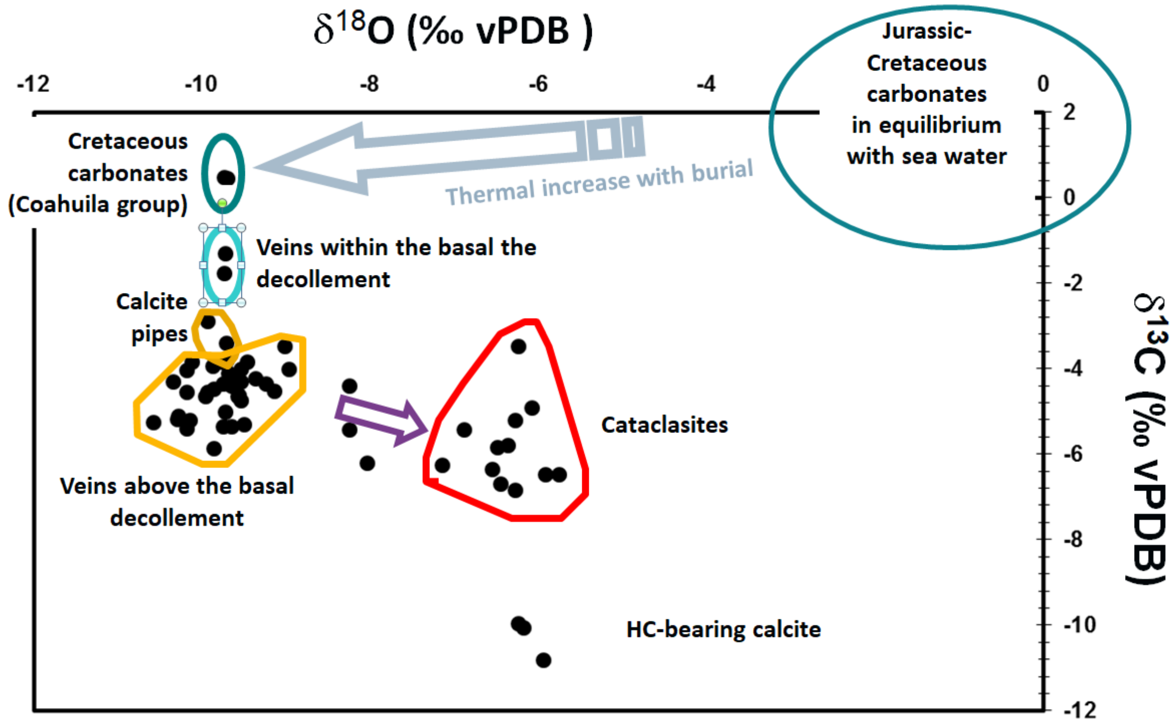

Fig. 26. Diagram $\delta^{18}O/\delta^{13}C$ of calcite cements in fractures of the Parras Basin. The low $\delta^{18}O$ values in the carbonates of the Coahuila group are consistent with a high burial. The carbonates cements of the calcite tubes and veins within the Parras shale located within and above the decollement precipitated in similar thermal conditions. Cataclasites show higher $\delta^{18}O$ corresponding to lower thermal conditions. The lowest $\delta^{13}C$ values of calcites above the decollement are probably related to an enrichment in light carbon during maturation of organic matter.

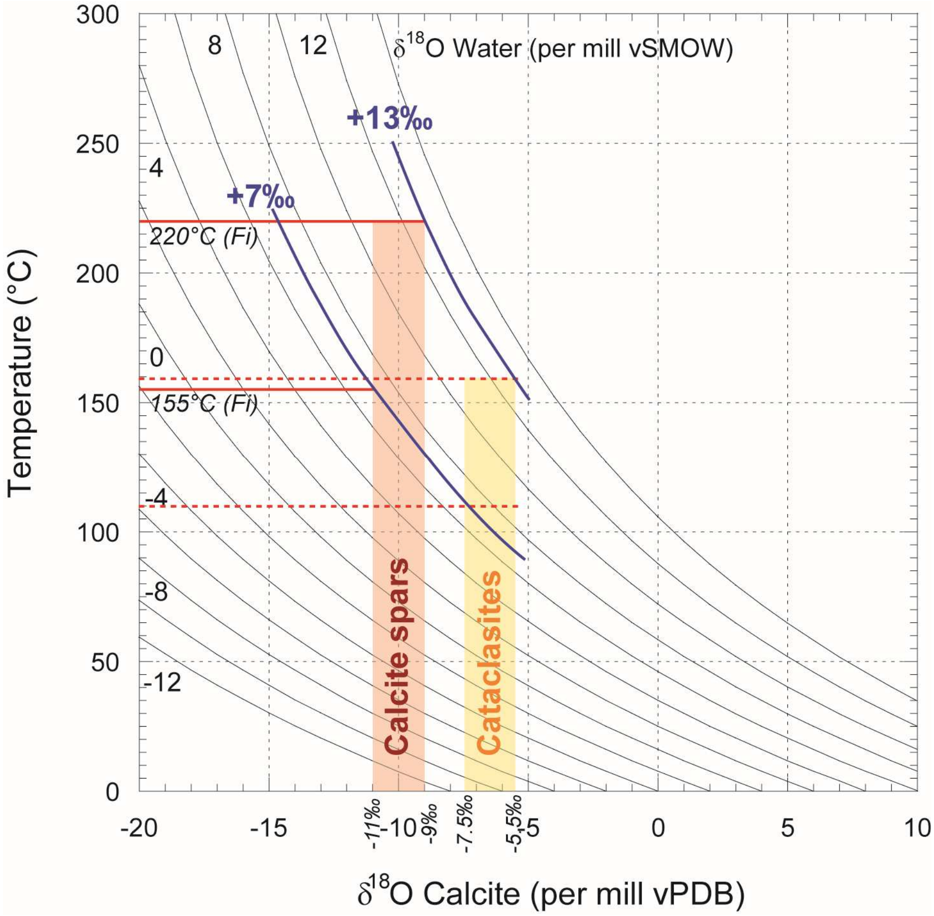

Fig. 27. Fractionation diagram for calcite in the calcite cements of the fractures of the Parras Shale (curves constructed with the equation of O'Neil et al., 1969). Crystallization temperatures of calcite (between 155 and 220°C) are obtained directly from the microthermometry study of fluid inclusions. Formation of cataclasites by crushing of former calcite spars is probably occurring at lower temperatures in the range of 110°-160° (see discussion in the text).

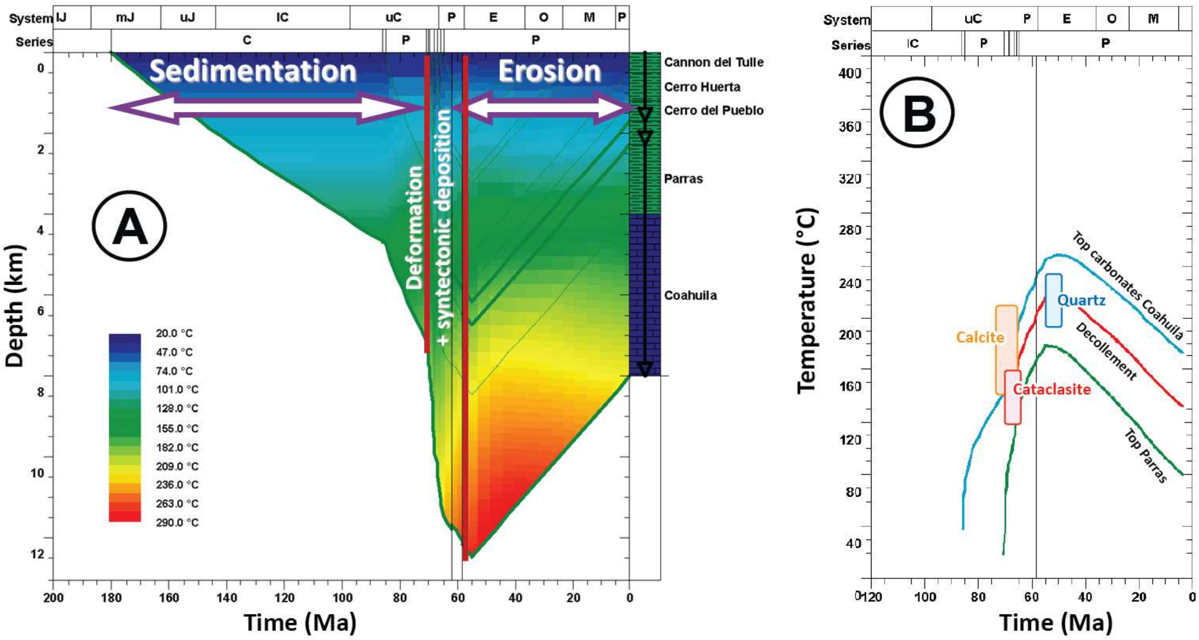

Fig. 28. A. The main stages of the modeled thermal history (lJ: Early Jurassic, mJ: Mid-Jurassic, uJ: Late Jurassic, lC: Early Cretaceous, uC: Late Cretaceous, P: Paleocene, E: Eocene, O: Oligocene, M: Miocene, P: Plio-Quaternary). A progressive increase of the temperature occurred during sedimentation, then an acceleration of the increase of temperature occurred in relation with higher sedimentation rates before contraction tectonics coupled with a syn-tectonic sedimentation, finally, a phase of cooling occurred linked to the erosion of the system. **B.** Syn-kinematic diagenetic events replaced within the thermal history. 1. Calcite precipitation associated with hydraulic fracturing and rapid percolation of hot fluids of deep origin (not in equilibrium with the host rocks in the decollement area but in equilibrium with the rocks Coahuila carbonates; hydrothermal type); 2. Cataclasites recrystallization at the thermal conditions of the host rocks in the decollement area (lower thermal conditions compared to calcite); 3. Quartz precipitation at the thermal peak.

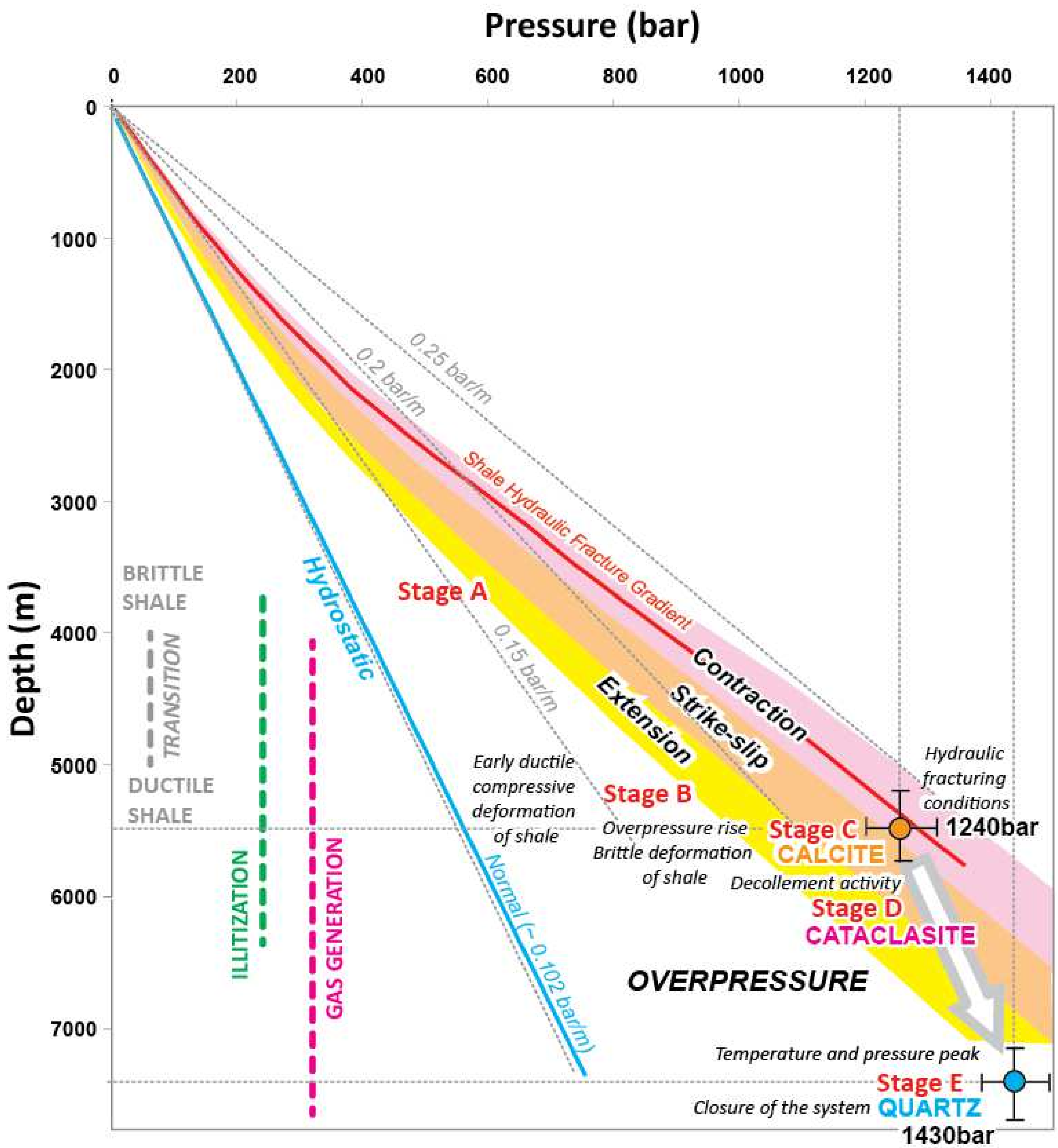

Fig. 29. Estimate of pressure-depth conditions for the sample 68A deduced from the study of fluid inclusions. On this graph, we also attempt to replace the different stages of deformation and diagenesis described in the text. The hydraulic fracturing conditions *versus* the structural context are estimated from a compilation of global values of minimum leak-off pressure from Grauls (1998) and Deville et al. (2010). The present case study corresponds to contraction conditions (minimum stress vertical).

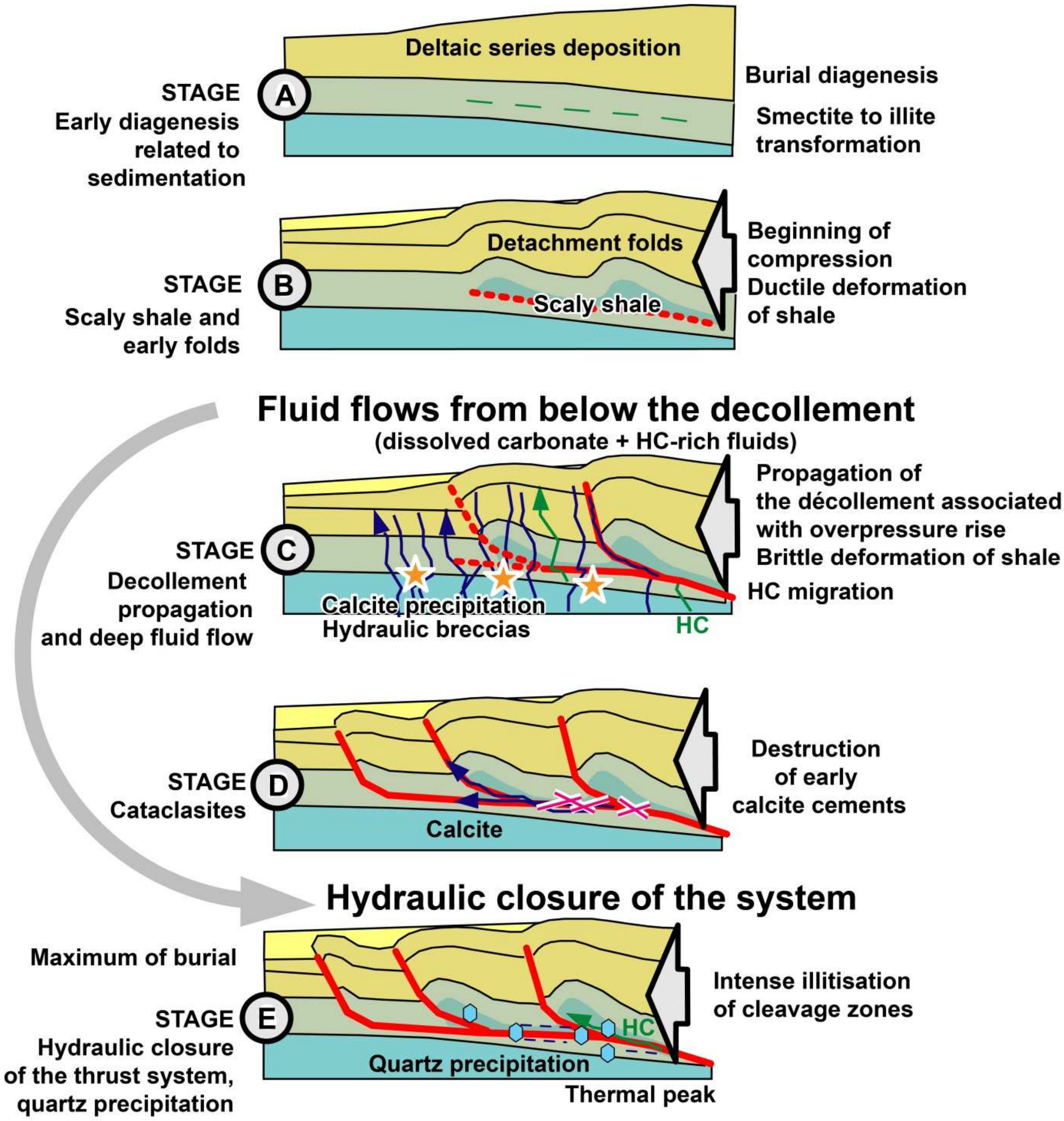

Fig. 30. Schematic model of deformation - fluid migration – diagenesis relationships.